Yukon University

Assessment and monitoring of a new retrogressive thaw slump at km 1456 of the Alaska Highway: A rare opportunity

May 2021

This publication may be obtained from:

YukonU Research Centre, Yukon University
500 University Drive P.O. Box 2799
Whitehorse, Yukon Y1A 5K4
867 456 6986 or 1 800 661 0504
www.YukonU.ca/research

Recommended Citation:

Calmels, F., Roy, L.P., Laurent, C., Amyot, F., Cubley, J., Lipovsky, P., 2021. Assessment and monitoring of a new retrogressive thaw slump at km 1456 of the Alaska Highway: A rare opportunity. YukonU Research Centre, Yukon University, 72 p.

Crown-Indigenous Relations and Northern Affairs Canada
Relations Couronne-Autochtones et Affaires du Nord Canada

Transports Canada
Transport Canada

Yukon

ArcticNet
ᐅᑭᐅᖅᑕᖅᑐᑦ ᑐᑭᓯᓂᐊᖅᑎᑦᑕ

Project Team

Contributing Authors

Fabrice Calmels	YukonU Research Centre
Louis-Phillipe Roy	YukonU Research Centre
Cyrielle Laurent	YukonU Research Centre
Frances Amyot	YukonU Research Centre
Joel Cubley	School of Science, Yukon University
Panya Lipovsky	Yukon Geological Survey

Prepared by

Frances Amyot	YukonU Research Centre

Acknowledgments

We appreciate the support of all participants and partners who have contributed to this project, including YG Department of Energy Mines and Resources (Land Planning and Agriculture Branches; YG Department of Highways and Public Works (Transportation Engineering Branch); YG Department of Environment (Water Resources Branch); YG Department of Community Services; and the City of Whitehorse (Engineering and Planning Departments). The site is on the traditional territory of Kwanlin Dün First Nation and Ta'an Kwäch'än Council.

Many thanks to the numerous field assistants who made this work possible, including Moya Painter, Daniel Jolkowski, Pamela Godin, Rebecca Irish, and Maude Bergeron-Lambert.

Funding for this project was provided by Transport Canada's Northern Transportation Adaptation Initiative (NTAI). Additional funding was provided by ArcticNet, as well as by Crown-Indigenous Relations and Northern Affairs Canada (CIRNAC) Climate Change Preparedness in the North (CCPN) program, which was administered by Yukon Environment's Climate Change Secretariat. In-kind contributions were also made by Yukon Geological Survey, Yukon University Research Centre and Yukon Government partners listed above.

Table of contents

1. Context of the survey: An introduction

1.1. General introduction

Retrogressive thaw slumps (RTS) are a form of slope failure resulting in a mass-wasting landform. This category of landslide results from the thawing of ice-rich permafrost, i.e., permafrost containing a significant amount of excess ice. RTSs usually begin when ice-rich permafrost is exposed because of erosion, mass movement, forest fires, construction, or mining. This exposed ground ice becomes visible and unprotected and can retreat retrogressive manner while the slumping of thawed soil occurs. A steep headwall thus develops (Figure 1). In more dramatic cases, the RTS is quickly enlarged by the slumping and a steep or vertical headwall develops leaving a low-gradient floor covered by slumped soil, a mixture of thawed sediment and meltwater that slides down the face of the headwall and flows as it retreats.

Retrogressive thaw slumps are common in ice-rich glaciolacustrine sediments and fine grained diamictons. Such is the case for an active RTS that was found adjacent to the Alaska Highway at km 1456 in April 2019 during a field study led in partnership with the Yukon Geological Survey (YGS). The slump developed on a hillslope along the shoreline of the Takhini River. In the area, permafrost is discontinuous and found in sporadic isolated patches that can be significantly ice-rich and thaw-sensitive. This RTS is located 200 m west of another RTS that was initiated prior to 1979 and was partially stabilized by 2004. Between these two features stands a wooded area showing signs of slope instability (collapsed trees, cracking) where a third RTS may soon develop (Figure 2).

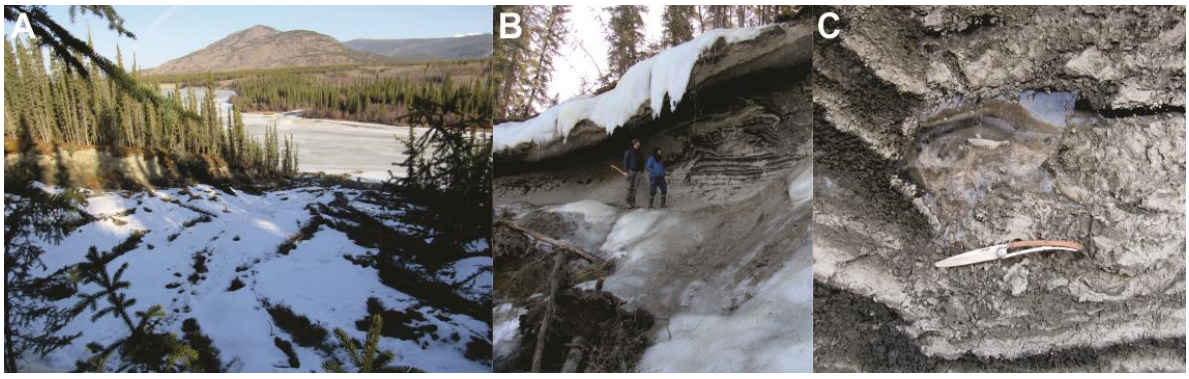

Figure 1. A) View of the RTS; B) Headwall of the RTS exposing ice-rich permafrost; C- 10 cm thick ground ice lenses

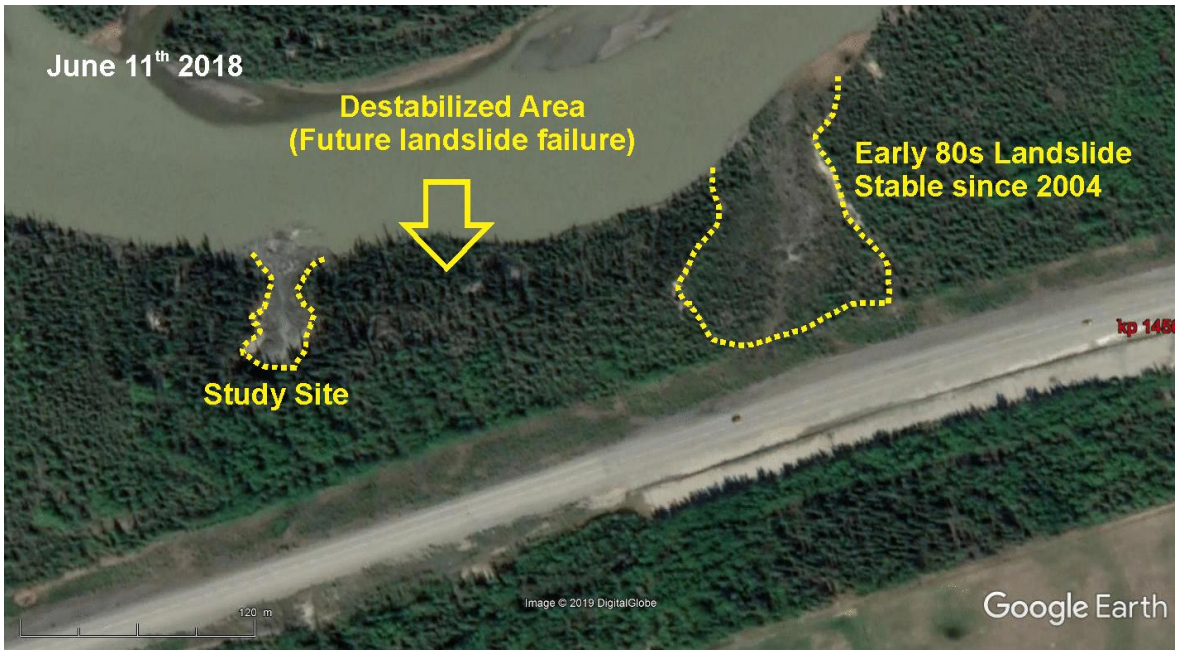

Figure 2. Study area at Km 1456 on the Alaska Highway

This is an alarming situation, but also one that presents an opportunity for climate change adaptation research, as well as outreach and engagement with Yukon transportation professionals, and Yukon University students. The RTS has been active for six or seven years (initiated in 2013 or 2014) based on an analysis of Google Earth satellite and aerial imagery. According to aerial imagery, the 1979 RTS remained active for 25 years, suggesting that this RTS will likely continue expanding during the next several summers, with the potential risk of it eventually impacting the road.

1.2. Study goals

The purpose of this study was to act before any serious damage occurs and seize the opportunity of the site being located near the city centre to develop an intensive research program at a low cost. The objective was to develop an innovative research program around this RTS site that will:

- Develop a better understanding of retrogressive thaw slumps that impact road corridors in the North;

- Develop and test a multi-technical monitoring approach using complementary instrumentation for RTSs that will eventually be used for the development of geohazard alarm systems;
- Inform an approach to mitigate the threat caused by RTSs on road corridors.
- Engage Yukon transportation professionals and Yukon University students in order to advance their understanding of the threats posed by RTSs; their lessons learned can then be applied to RTSs in more remote locations.

To reach this objective, several research activities were carried out on site, including:

- Drilling of sampled boreholes, from RTS to the right of way, instrumented with ground temperature cables, soil moisture sensors, and inclinometer arrays to monitor ground parameters and RTS failure in real-time;
- Monitoring ground surface movement with differential GPS (DGPS) measurement tying in with benchmarks and existing legal survey pins and establishing surface survey monuments;
- Imaging and topography monitoring using UAV (drone) photogrammetry;
- Two-dimensional Electrical Resistivity Tomography (ERT) surveying;
- Testing a new geophysical approach using 3D ERT and 3D Electromagnetic (EM) surveys to map permafrost properties and ground water movements;
- Mapping and monitoring of the propagation of tension cracks, and other ground movement markers as precursory indicators of failure.

The study addresses key knowledge gaps in mapping of RTS formation and evolution processes, as well as methodological gaps in the monitoring of such geohazards. To develop understandings of RTS processes, the survey focuses on 4 parameters:

- Frozen soil properties (through borehole data such as grain-size distribution, excess ice content, geophysics - ERT, etc.): which provides geotechnical information such as thaw sensitivity and potential consolidation;
- Ground thermal regime (borehole monitoring): which provides information such as ground temperature, active layer thickness, thaw rates, indications of water movement;

- Ground water dynamics (borehole monitoring/humidity sensor): which provides links between ground moisture, environmental conditions, and the timing and rate of the failure;
- Ground movements (below ground surface using inclinometers in boreholes; above ground surface including DGPS monitoring, UAV surveys, mapping of ground movement indicators): which provides information on the rate of deformation as well as its spatial distribution in three-dimensions.

The project monitored these parameters in real-time through the implementation of an array of sensors located in two boreholes instrumented with ground temperature cables, moisture sensors, and inclinometer arrays. One 20-25m borehole was drilled in the right of way (ROW), about 50 m from the location of the RTS headwall at the time of the drilling, to monitor failure indicators at a distance from the RTS during multi-year monitoring. The intention is to provide long term monitoring for signs of instability at depth. This monitoring station could be upgraded with warning and alarm systems in the future as part of a safety plan for monitoring the instability as it progresses towards the highway. A second, 6 m borehole was located close to the RTS (5-6 m from the headwall) to monitor the parameters during RTS failures. This borehole was checked regularly to recover the instrumentation when the RTS headwall retreated to the location of the borehole. Another 6-m borehole was attempted at an intermediate position, between the ROW borehole and the RTS borehole. However, ground conditions were such that it was not possible to drill deeper than 3 m.

Electrical resistivity tomography (ERT) surveys were conducted to complement borehole observations, characterize ice-rich permafrost thickness, distribution, and boundaries, as well as identify ground water movements. An innovative approach was developed, combining 3-dimentional ERT and electromagnetic (EM) surveys.

DGPS monitoring of an array of benchmarks, matched with UAV imagery monitoring provided a complete assessment of ground surface movement that can be integrated with geophysics and borehole data to provide a complete 3D representation of the RTS development, integrated in a geo-database.

This project provides information that will be used to model RTS processes, determine the relationships between the variety of measured parameters and the timing/rate of RTS failure. Ultimately, the information will be used to monitor other RTSs that impact transportation systems, and to design a system that could anticipate failure and alert highways operators. To the best of our knowledge, this type of multidisciplinary approach has never been used for characterizing and monitoring RTS formation processes.

2. Study area

2.1. General site description

The Takhini River retrogressive thaw slump site is located at kilometre 1456 of the Alaska Highway, approximately 30 km west of Whitehorse (Figure 3). The site is situated in the Takhini valley in the sporadic discontinuous permafrost zone, along the Takhini River. In 2014, a large retrogressive thaw slump developed along the Tahkini River bank, and has progressively moved towards the highway. The slump will likely continue to move towards the highway, which could eventually result in the collapse of the highway.

The retrogressive thaw slump was initiated by the erosion on the outer bend of a meander of the river. A tributary creek and alluvial fan enter the Takhini River on the opposite bank, which forces the river further to the outside on this bend. Nine other failures of the same type have occurred within 6 km of this location, including a 40 000 m^3 retrogressive thaw slump, only 180 metres east of this site. This last thaw slump was initiated in 1979 by river bank erosion and stayed active until 1986 when the slumping led the headscarp to retreat 112 m to approximately its present position. Since 2004, that thaw slump stabilized a few metres short of the highway. However, cracks in the road surface are continuing to propagate parallel to the landslide headscarp. The active retrogressive thaw slump has been retreating towards the highway at an average rate of 8 metres per year since 2014. Since then, several multi-metre long tension cracks have formed between the failure and the road, the closest being 20 metres from the road embankment.

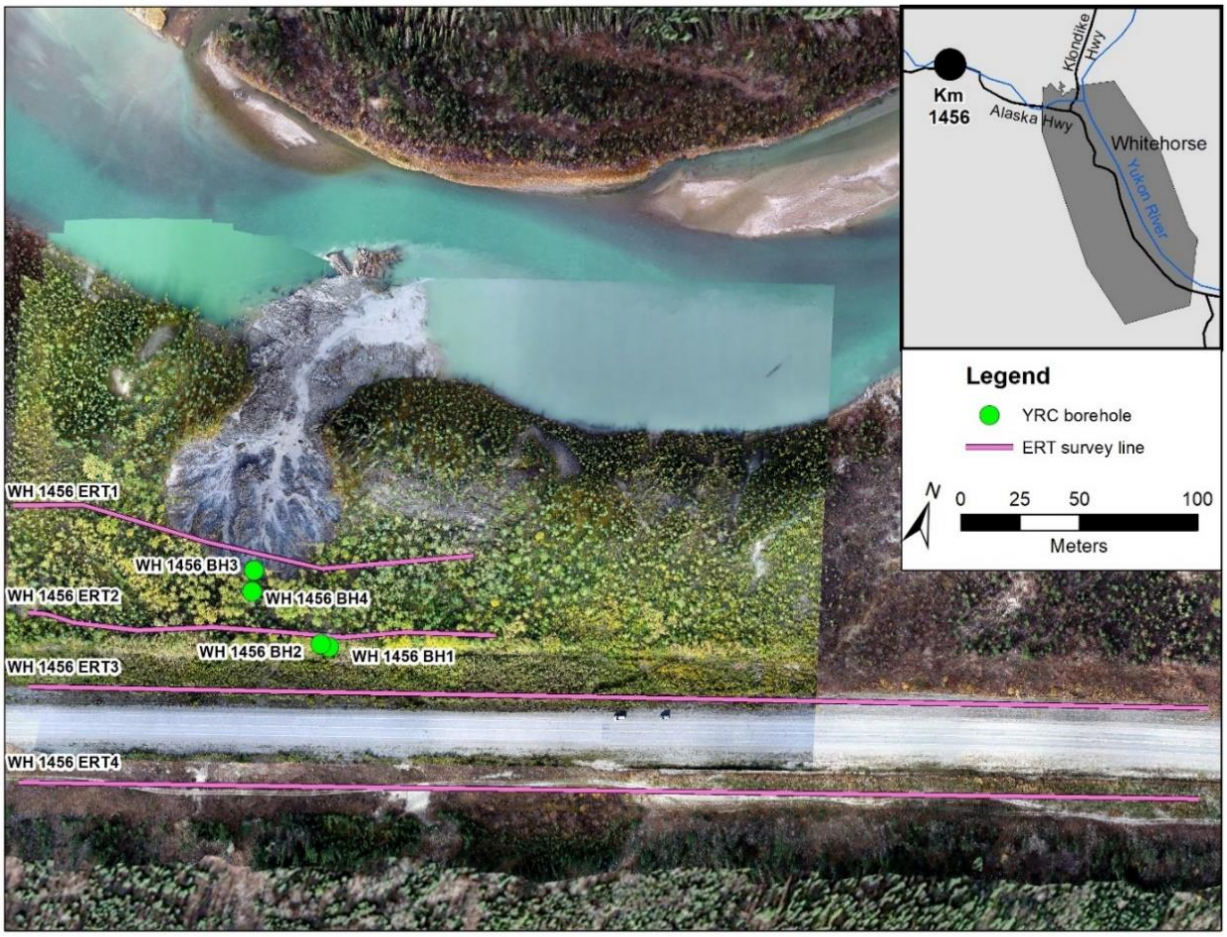

Figure 3. Location of the Alaska Highway km1456 retrogressive thaw slump with borehole and geophysical survey locations

2.2. Climate and vegetation

This section of the Alaska Highway is located in the Southern Lakes Ecoregion. The climate is subarctic with large seasonal variations in temperature and a mean annual air temperature (MAAT) of -3.0 °C, which is 2.3°C cooler than the Whitehorse airport (Burn, 1998). This area is also characterized by low precipitation and low humidity due to the rain shadow of the Coast Mountains. The deciduous mixed forest consists of lodgepole pine (*Pinus contorta*), white spruce (*Picea glauca*), and trembling aspen (*Populus tremuloides*) (Figure 4). Shrubs such as willow (*Salix spp.*) and soapberry (*Shepherdia canadensis*) are present throughout much of the site. Common plant species are forbs

such as fireweed (*Chamaenerion angustifolium*) and alpine sweet-vetch (*Hedysarum alpinum*), mosses, and lichens such as *Cladonia spp*.

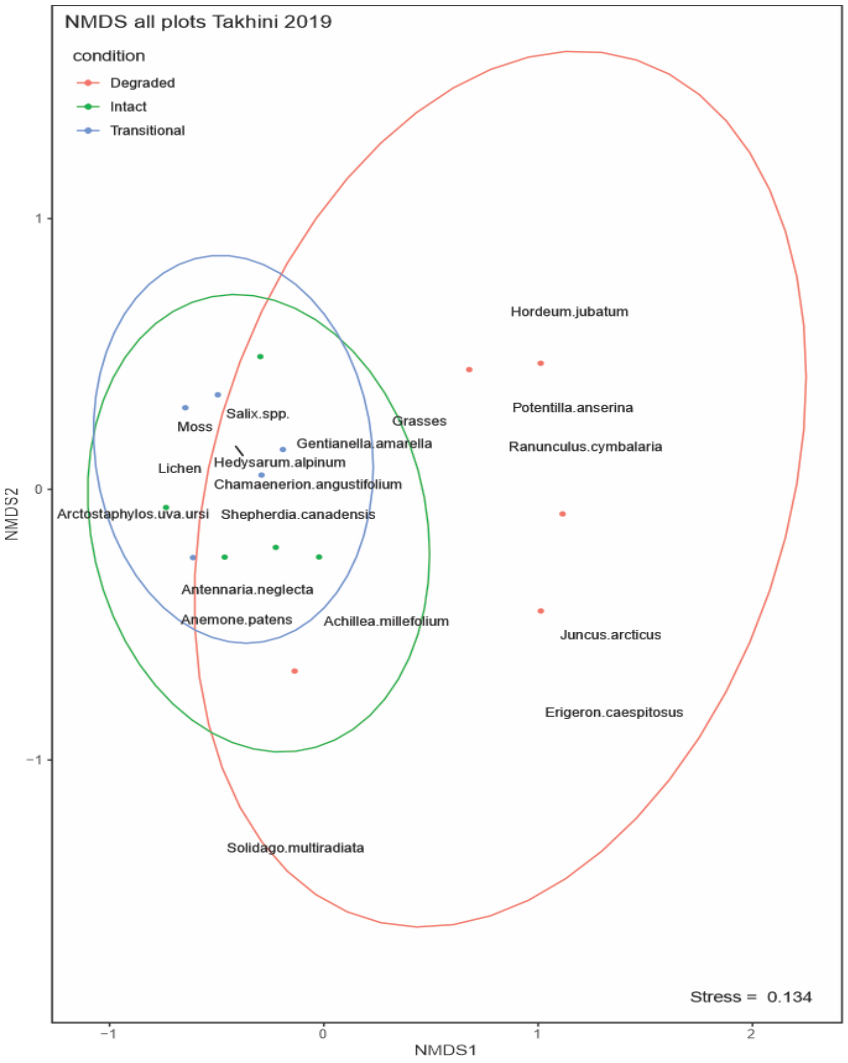

Figure 4. Vegetation plots comparing distribution with ground conditions

2.3. Geology

The entire study area is underlain by Jurassic Richtofen Fm, as part of the Whitehorse Trough sedimentary basin (200-168 Ma). The Richtofen formation is a mix of turbiditic sandstone-siltstone-mudstone, plus conglomerate (Yukon Geological Survey, 2020).

The surficial geology and landscape features of the study site are largely a product of the most recent (Late Wisconsinan) McConnell Glaciation, which occurred between 24,000 and 11,000 years ago (Figure 5). Deglaciation of lowland areas began approximately 14,000 years ago. During deglaciation, large volumes of meltwater were dammed in some valleys and formed large glacial lakes. In the Takhini River, Glacial Lake Champagne deposited up to 75 m of silt and clay between 9,000 and 10,000 years ago. Glaciolacustrine silt and clay commonly contain massive ice bodies and are prone to retrogressive thaw slides and thermokarst degradation when disturbed by river erosion, forest fires, or other changes in surface conditions.

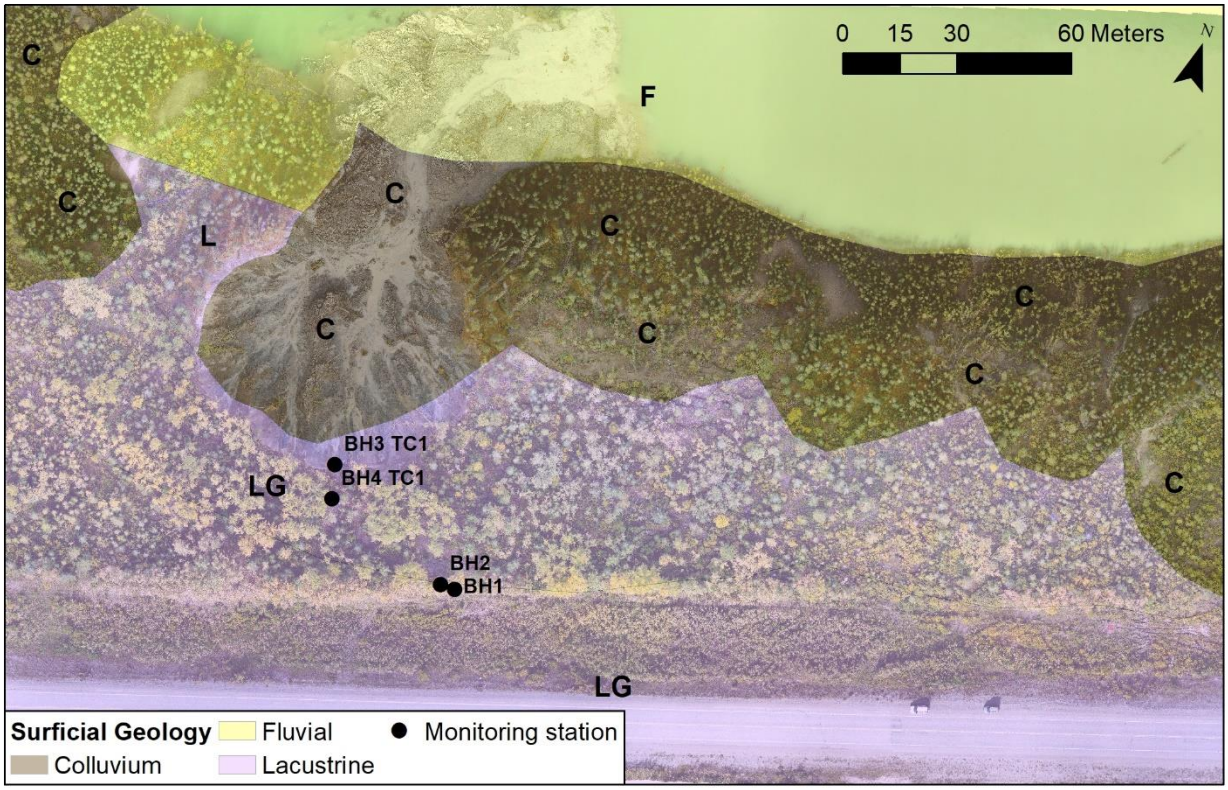

Figure 5. Surficial geology at Takhini retrogressive thaw slump site (YGS, 2021)

2.4. General permafrost and ground conditions

The only signs of permafrost degradation noticeable on site in the forested area are those associated with the development of the retrogressive thaw slump. These include metre wide tension cracks and split trees due to ground movements. Along the road in

the cleared area, some shallow ponds are present, which probably have thermokarstic origins.

Retrogressive thaw slumps occur when ice-rich permafrost thaws, and generally form on hillslopes. They usually occur along the shorelines of lakes, rivers, and coastlines. Generally, they occur in areas underlain by massive ice bodies, or ice-rich silts. Retrogressive thaw slumps are very similar to landslides in more temperate regions, although they do not have a failure surface. They are typically fast-developing features but tend to be short-lived: most retrogressive thaw slumps stabilize between 30 and 50 summers after their initiation (French and Egginton, 1973). Retrogressive thaw slumps represent one of the most rapid erosive processes operating in present-day periglacial environments.

3. Methods

3.1. Geotechnical boreholes

3.1.1. Boreholes

A total of four boreholes of various depths were dug at the site, using a variety of methods outlined below. These boreholes were outfitted with multiple sensors, as discussed in sections 3.1.3, 3.1.4, and 3.1.5 below. Table 1 outlines the specifics of the boreholes.

Table 1. Geotechnical boreholes

Site	Date	Coordinates (UTM)	Depth	Sensor Depths
WH_1456_BH1	16/10/2019	8 V 471985 6746876	10 m	No sensors were installed
WH_1456_BH2	23/10/2019	8 V 472000 6746887	25 m	Temperature: AT, 0, 0.5, 1.0, 1.5, 2.0, 3.0, 4.0, 5.0, 6.0, 7.0, 8.0, 9.0, 10.0, 15.0, 20.0 m.

				Inclinometer: every 50 cm from 0 to 20.0 m
WH_1456_BH3	13/05/2020	8 V 471970 6746905	6 m	Temperature: 0, 0.5, 1.0, 2.0, 3.0, 4.0, 5.0, 6.0 m. Inclinometer: every 50 cm from 0 to 6.0 m. Soil Moisture: 0.5, 1.0, 2.0, 3.0, 4.0, 5.0, 6.0 m.
WH_1456_BH4	22/05/2020	8 V 471973 6746893	3 m	No sensors were installed

Borehole BH1 (WH_1456_BH1) and BH2 (WH_1456_BH2) were drilled on October 16th and 23rd 2019, respectively, by Midnight Sun Drilling under the supervision of Louis-Philippe Roy and Panya Lipovsky, as seen in Figure 6. The purpose of WH_1456_BH1, was to provide a relatively complete cryostratigraphical record and geotechnical assessment of permafrost in the area and better estimate the risk that the RTS poses on the Alaska Highway. The location of WH_1456_BH1 was selected based on ERT survey WH_1456_ERT2, which showed indications of ice rich sediments at this location. At 10 metres depth, a point of refusal was reached in unfrozen clayey silt sediment. The wall of the borehole started to collapse due to the amount of water intercepting the borehole, threatening to trap the CRREL core barrel in the borehole. WH_1456_BH2 was drilled 2 metres away from WH_1456_BH1 using a Hollow Stem destructive drill to reach the target depth of 25 metres. Once drilling was completed, the boreholes were cased with two 1-inch PVC conduit, and backfilled to the surface using fine gravel and bentonite.

Figure 6. Midnight Sun Drilling CRREL drill rig and permafrost cores (WH_1456_BH1)

Two shallow boreholes, BH3 (WH_1456_BH3) and BH4 (WH_1456_BH4) were drilled in the late spring of 2020 by the Permafrost and Geoscience department of the Yukon University Research Centre (YRC) (Philippe Roy, Fabrice Calmels and Cyrielle Laurent). WH_1456_BH3 was drilled on May 13th, 2020, 10 metres beyond the headwall of the RTS. The borehole was created by removing the unfrozen active layer using a shovel down to the thaw front (31 cm). The borehole was drilled using a GÖLZ MT portable core-drill system down to 6.0 metres. The GÖLZTM portable core-drill system is a light hand drill with a high rotation speed (600 rpm) that can be controlled by two people and is therefore used with minimal impact on the environment. Stainless steel rods measuring 1 m in length and 4.5 cm in diameter, and a core barrel 40 cm long and 10 cm in diameter were used, making it possible to drill up to 5 m into unconsolidated, fine to medium grained material (sand to clay). A core catcher was used to extract the frozen core out of the borehole, which allows for continuous undisturbed permafrost sampling.

Once drilling was completed, the borehole was cased with two 1-inch PVC conduits, and backfilled to the surface. This location was specifically chosen close to the headwall so that the conditions leading to failure could be recorded and analyzed to better understand the initiating factors of rapid slump movements. Borehole failure occurred on August 12th 2020, as seen in Figure 7.

Figure 7. WH_1456_BH3 (BH3) failure, image taken on August 13th 2020

WH_1456_BH4 was drilled on May 22nd 2020, 12.6 metres south of WH_1456_BH3 and 23 metres beyond the headwall of the RTS, between the ROW and the slump. The borehole was created by removing the unfrozen active layer using a shovel down to the thaw front (50 cm). The borehole was drilled using a GÖLZ MT portable core-drill system down to 2.97 metres where a point of refusal was reached. The dry nature of the sediment made it extremely hard for the core barrel to cut through the material. Once drilling was completed, the borehole was cased with a 1-inch PVC conduit, and backfilled to the surface.

3.1.2. Grain size, ice content and borehole log analysis

Cores were extracted from WH_1456_BH1 and WH_1456_BH3 allowing for laboratory analyses to measure geotechnical properties of the active layer and permafrost samples. Soil grain characteristics, ice characteristics as well as plasticity index, remolded bulk density, porosity, specific gravity, and thaw settlement potential were calculated for representative samples. To evaluate ice characteristics in permafrost samples, the cryostructure, volumetric ice content, gravimetric ice content and settlement potential were quantified. The specific methods for these analyses are described below. A log for each permafrost borehole was then created by assembling laboratory photos of the cores. Borehole logs include maximal depths, grain size ratio and volumetric excess ice content.

3.1.2.1. Grain size analysis

Sieve and hydrometer analyses of grain size were performed following a specifically modified American Standard and Testing Method protocol (ASTM D422-63, 2000). The sieves used were 4, 2, 1, 0.5, 0.25, 0.125 and 0.063 mm. The data was then compiled in GRADISTAT to generate the statistical analysis and integrated into the borehole log.

3.1.2.2. Ice characteristic analysis

Ice characteristics were assessed by evaluating the cryostructure, as well as measuring the gravimetric ice content, the volumetric ice content, and the volumetric excess ice content, which are described in more detail below.

3.1.2.2.1. Cryostructure

The cryostructure of the cores was described *in situ* during the drilling process, using standard terminology (Stephani et al., 2010; Murton and French, 1994). The classification was validated with the visual analysis of high-resolution pictures of each sample taken in the field.

3.1.2.2.2. Gravimetric ice content

Gravimetric ice content was calculated using the following equation:

$$u_I = \frac{(M_I)}{(M_S)}$$

where M_I is the ice weight (measured as weight loss after drying (g)) and M_S is dry soil weight (g). Results are expressed as percentages (dimensionless).

3.1.2.2.3. Volumetric ice content

Volumetric ice content was measured using a water displacement method. The frozen sample was weighed and lowered into a four-inch diameter PVC tube filled with 1.5 L of water. Water was then extracted from the tube until the initial water level (1.5 L) was achieved. The amount of water displaced was measured using a 250 mL graduated cylinder with a precision of ±2 mL. The sample was then removed from the tube, placed in a clean tin tray, and dried completely in a drying oven at 60°C. The dry sample was

then weighed, crushed using a mortar and pestle, vacuum sealed in a clear plastic bag, and labelled according to the borehole and sample increment. The volumes of the vacuum-sealed dry samples were measured using the same methods as the frozen cores, and the volume of the vacuum bags was subtracted from the measurement to obtain a dry sample volume. Assuming the density of ice to be 1.09 cm^3/g, the volumetric ice content was calculated using:

$$IVC_{(\%)} = \left(\frac{Wc \times 1.09}{Vtot}\right) \times 100$$

where W_c is the water mass content and V_{tot} is the total (frozen) core volume. Results are expressed as percentages. For the consolidation test samples, the volume has been measured using Glycol displacement. This allowed the possibility to keep the samples under 0°C and avoid the use of vacuumed sealed bags. The volume of excess ice content was calculated using:

$$V_{ice} = V_{tot} - V_{sed}$$

where V_{tot} is the total frozen core volume and V_{sed} is the dry soil volume. The volumetric excess ice content (V_{ice}) is then divided by the total frozen core volume (V_{tot}) and expressed as a percentage (fundamentally meaning cm^3/cm^3). This method is valid for mineral soils only.

3.1.3. Ground temperature and environmental conditions

As mentioned in section 3.1.1, only boreholes WH_1456_BH02 (BH2) and WH_1456_BH03 (BH3) were outfitted with ground temperature sensors (Table 1). Borehole BH2 was instrumented with a 16-channel LogR Systems thermistor and logger to record ground temperatures at 0, 0.5, 1.0, 1.5, 2.0, 3.0, 4.0, 5.0, 6.0, 7.0, 8.0, 9.0, 10.0, 15.0, 20.0 m of depth. The piping was filled with silicone oil to improve the accuracy of the temperature readings. Recording began on February 28th, 2020 at 24:00 and data were last downloaded on December 30th, 2020. Therefore, there are 10 months of ground temperature data available for this borehole.

Borehole BH3 was instrumented with two 4-channel Hobo UX120 loggers to record ground temperatures at 0, 0.5, 1.0, 1.5, 2.0, 3.0, 4.0, 5.0, 6.0 m of depth. The piping was

also filled with silicone oil to improve the accuracy of the temperature readings. Recording began on June 1st, 2020 at 18:00 and ended on August 12th, 2020 at 08:00, after a major slumping event caused the slump to retreat beyond the location of the borehole, releasing the piping in the process.

To complement ground temperature data from the thermistors, air temperature and other climatic variables such as precipitation were downloaded from Environment and Climate Change Canada for the Whitehorse Airport.

3.1.4. Inclinometer

Borehole WH_1456_BH02 was instrumented with a MeasureAnd SAAV Shape Array inclinometer to monitor deformation and slope movements every 50 cm from the surface to 20 m of depth, for a total of 41 reading depths. Recording began on April 17th, 2020 and data were last downloaded on December 30th, 2020.

Borehole WH_1456_BH03 was also instrumented with a MeasureAnd SAAV Shape Array inclinometer to monitor deformation and slope movements every 50 cm from the surface to 6m of depth, for a total of 13 reading depths. Recording began on June 4th, 2020 at 18:00 and ended on August 12th, 2020 at 08:00, after a major slumping event caused the slump to retreat to the location of the borehole, releasing the piping in the process.

The data were downloaded and processed in the MeasureAnd software SAASuite to convert the data to deformation and deviation values.

3.1.5. Soil moisture

Borehole WH_1456_BH03 was outfitted with METER EC-5 soil moisture sensors at 0.5, 1, 2, 3, 4, 5 and 6 m of depth, and a CR1000X data logger. Recording began on June 1st, 2020, and ended on August 12th, 2020 at 08:00, after a major slumping event caused the slump to retreat to the location of the borehole, releasing the piping in the process. Due to uncertainties in the sensor's programming, the percentage of soil moisture cannot be assessed. However, by rescaling the data to values between 0 and 1, the moisture values can be compared across the data set to expose any trends. To do so, the min-max normalization method was used, according to the following equation:

$$X_{norm} = \frac{x - x_{min}}{x_{max} - \mathrm{x}_{min}}$$

Where X_{norm} is the scaled value of soil moisture;

x_{min} is the minimum value of x across the dataset;

And x_{max} is the maximum value of x across the dataset.

3.2. ERT and EM

3.2.1. Brief introduction to methodologies and novel use of 3D

The specific objective of the 3D geophysics surveys was to perform three-dimensional electrical resistivity tomography (ERT) and electromagnetic (EM) surveys of a square area between the headwall of the RTS and the highway to develop a better understanding of ground ice distribution as well as the groundwater movements occurring within the RTS area.

3.2.2. ERT

Electrical resistivity tomography (ERT) is a geophysical method that passes electrical current through stainless steel electrodes that are driven into the ground surface. A terrameter located at a central "station" measures the resistivity distribution of the subsurface between electrode pairs. Resistivity is the mathematical inverse of conductivity and indicates the ability of an electrical current to pass through a material. Mineral materials are mostly non-conductive, with the exception of specific metallic ores, and some clays. Therefore, variation in the resistivity of a soil or rock profile is governed primarily by the amount and resistivity of pore water present in the profile, and the arrangement of the pores. This makes ERT very well suited to permafrost and hydrology applications. Because most water content in frozen ground is in the solid phase and typically has a higher resistivity than unfrozen water content, permafrost distribution can be inferred based on changes in resistivity between frozen and unfrozen ground.

An ERT system consists of an automated imaging unit and a set of wires connected to an electrode array. The system used for the surveys presented in this report is an ABEM Terrameter LS electrical resistivity and tomography system, consisting of a four-channel imaging unit and four electrode cables, each with 21 take-outs at five-metre intervals. To

conduct a survey, 81 electrodes are driven into the ground along a survey line and connected to the electrode cables (Figure 8).

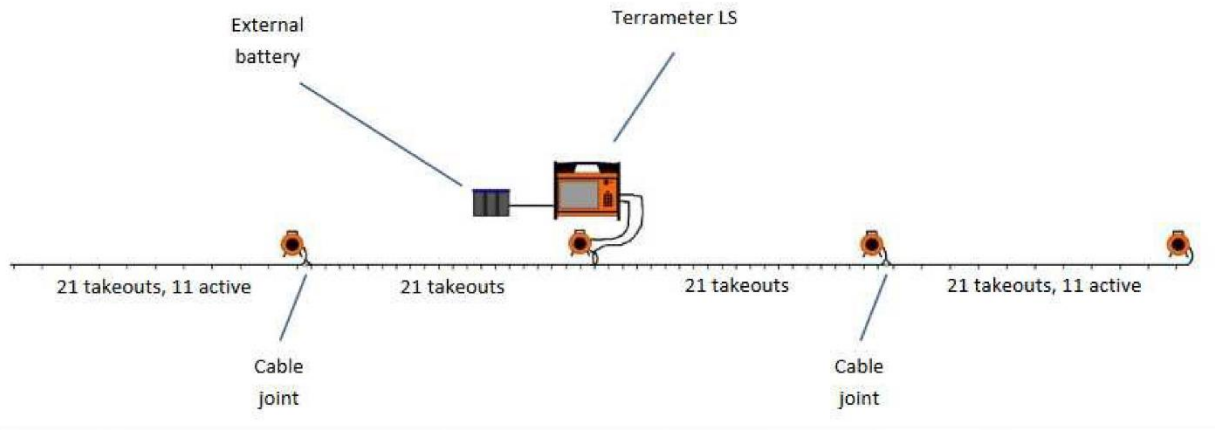

Figure 8. Instrument set-up for ERT surveying

Two different types of electrode configurations or arrays were used during the surveys: the Wenner and dipole-dipole arrays. These arrays differ in how they pair current and potential electrodes (Figure 9). A direct current electrical pulse is sent from the resistivity metre along the survey line in two current electrodes (C1 and C2), and the measurement is performed by two potential electrodes (P1 and P2). The resulting data consists of a cross-sectional (2D) plot of the ground's resistivity (ohm·m) versus depth (m) for the length of the survey.

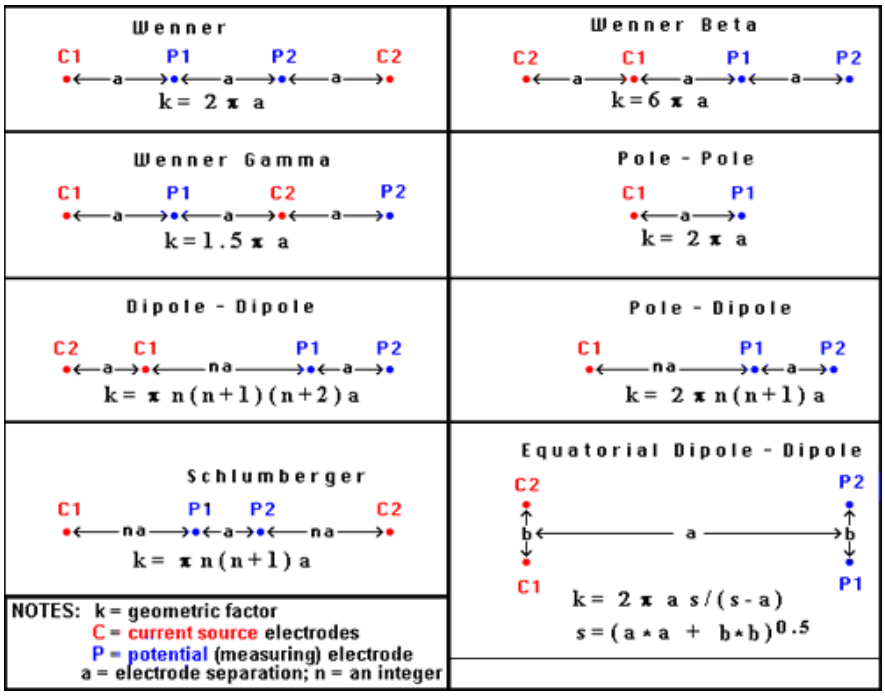

Figure 9. Survey configurations or "arrays" for ERT surveying

In general, the Wenner array is good in resolving vertical changes (i.e. horizontal structures), but relatively poor in detecting horizontal changes (i.e. narrow vertical structures). Compared to other arrays, the Wenner array has a moderate depth of investigation. Among the common arrays, the Wenner array has the strongest signal strength. This can be an important factor if the survey is carried in areas with high background noise. Relatively small current magnitudes are needed to produce measurable potential differences. The disadvantage is that to image deep into the earth, it is necessary to use longer current cables. The Wenner array is also very sensitive to near surface inhomogeneities which may skew deeper electrical responses. One disadvantage of this array for 2-D surveys is the relatively poor horizontal coverage as the electrode spacing is increased, which can be a problem when using a system with a relatively small number of electrodes.

The dipole-dipole array is very sensitive to horizontal changes in resistivity, but relatively insensitive to vertical changes in the resistivity. That means that it is good for mapping vertical structures, such as dykes and cavities, but relatively poor in mapping horizontal structures such as sills or sedimentary layers. This array can have a shallower depth of investigation compared to the Wenner array, but it has better horizontal data coverage than the Wenner, which can be an advantage when the number of nodes available with

the multi-electrode system is small. One possible disadvantage can be a very small signal strength. With the proper field equipment and survey techniques, this array has been successfully used in many areas to detect structures such as cavities where the good horizontal resolution of this array is a major advantage.

There is no single model that fits the observed resistivities. Instead, the modelled results converge by iteration with the measured values. The choice of when to stop iteration in the RES2DINV software is made by the operator. Too few iterations lead to large Root Mean Square (RMS) errors (i.e., the model does not fit the measurements). Too many iterations can result in model 'over-fit' in which the broad patterns are lost. Analyses for this study were stopped after the 4th iteration as RMS errors were all very low (less than 5%) by that point. The profiles are presented with a linear depth scale and no vertical exaggeration. ERT profiles were interpreted in conjunction with the results of frost probing along the profiles, field descriptions of vegetation cover at the site, borehole and laboratory analyses undertaken by the research team, and surficial mapping. Results of the surveys are post-treated and analyzed at the YRC using inversion software (Res2DInv 64 and Res3DInv 32).

The specifications for the ERT surveys are shown in Table 2 below, and their locations in Figure 10 below.

Table 2. ERT survey specifications

WH_1456_ERT 1	30/5/2019	Dipole-Dipole & Wenner	Length: 200 m	Electrode Spacing: 2.5 m
0 m 50 m 100 m 150 m 200 m		8 V 472063 6746934 8 V 472017 6746915 8 V 471969 6746906 8 V 471919 6746905 8 V 471871 6746896		
WH_1456_ERT 2	27/06/2019	Dipole-Dipole & Wenner	Length: 200 m	Electrode Spacing: 2.5 m
0 m		8 V 472080 6746905		

50 m 100 m 150 m 200 m		8 V 472034 6746889 8 V 471985 6746876 8 V 471938 6746862 8 V 471887 6746857		
WH_1456_ERT 3	20/08/2019	Dipole-Dipole	Length: 500 m	Electrode Spacing: 2.5 m
0 m 100 m 200 m 300 m 400 m 500 m		8 V 471908 6746785 8 V 472003 6746814 8 V 472098 6746843 8 V 472194 6746871 8 V 472290 6746898 8 V 472385 6746927		
WH_1456_ERT 4	11/9/2019	Dipole-Dipole	Length: 500 m	Electrode Spacing: 2.5 m
0 m 100 m 200 m 300 m 400 m 500 m		8 V 471900 6746826 8 V 471998 6746853 8 V 472093 6746880 8 V 472184 6746907 8 V 472280 6746935 8 V 472378 6746964		

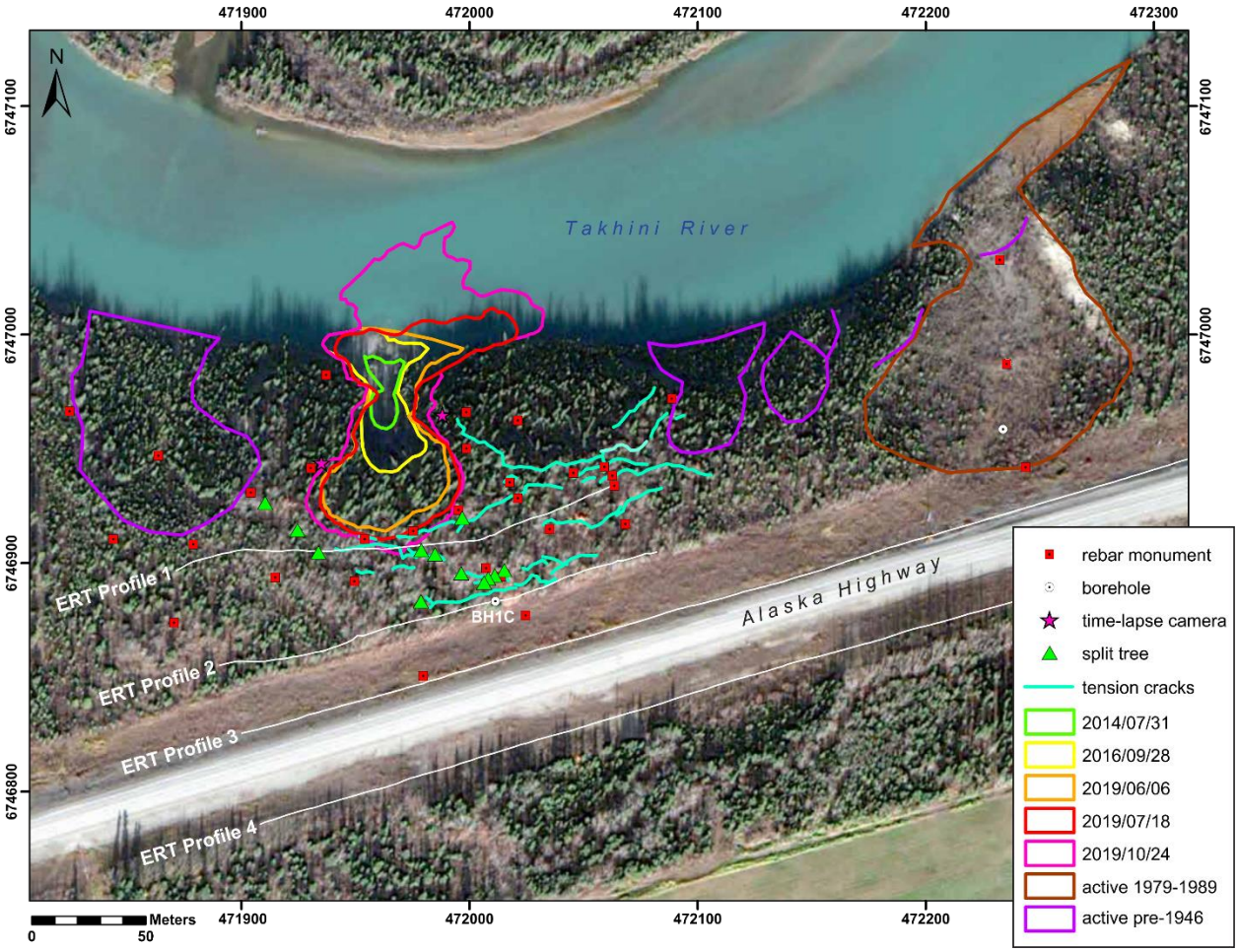

Figure 10. Field site with ERT survey lines

3.2.3. 3D Surveys

The approach merges two techniques, electrical resistivity tomography (ERT) and electromagnetic (EM). EM systems are used to measure electrical ground properties by investigating conductivity. Consisting of a transmitter and a receiver these instruments are suited for mineral exploration and geological mapping, but also can be used in permafrost science, in a similar way to ERT. The EM System has the advantage of being a quicker acquisition technique, but it has not been tested thoroughly in permafrost environments compared to ERT. By acquiring measurements following a grid pattern on the investigated zone, the Yukon University system can be used to develop a 2D mapping of EM properties of the underground using 3 frequencies at the same time, i.e., to produce three 2D horizontal EM maps at 3 different depths at once. The three 2D maps,

or slices, are then integrated together to produce a 3D model of the EM properties for the investigated area, where any vertical and/or horizontal slices of the EM properties can be extracted and interpreted.

By calibrating and comparing EM data with borehole and ERT data, the project aims to map and assess ground conditions that may play a role in the RTS development: thickness of the active layer, thermal state of the ground (frozen/unfrozen), presence of ground ice; groundwater movement patterns (absence/presence).

A 40 by 40 m grid with data acquisition nodes located every two metres, was designed in ArcGIS based on UAV imagery. The grid was then set up on site using stakes and cords, and nodes were surveyed with a DGPS (Figure 11).

Figure 11. Grid used for EM and 3D ERT surveys

3.2.3.1. 3D ERT

For the 3D ERT survey, the ABEM Terrameter only used one electrical cable with 21 take-outs at two-meter intervals to acquire 21 parallel ERT surveys located two metres apart along 20 m survey lines. Each node corresponding to the location of an electrode, the 21 surveys covered the entire 40 m x 40 m grid. The twenty-one 2D ERT profiles were created using a dipole-dipole array following the east-west direction. The resulting data consists of a cross-sectional (2D) plot of the ground's resistivity (ohm·m) versus depth (m) for the length of the survey.

After field data acquisition, RES3DINV software was used to integrate the 21 surveys and produce a three-dimensional resistivity (3D) resistivity model. RES3DINV is a computer program that automatically determines a 3D model for the subsurface using the data obtained from the 3D electrical imaging survey. The process was facilitated by the fact that electrodes were arranged in an orthogonal grid. While RES3DINV produces 3D model data, it does not produce 3D rendering, and only allows for the visualization of 2D resistivity profile. For 3D rending, Voxler, a 3D graphics package by Golden Software, was used. The 3D graphics suite also allowed to for the combination of the ERT and EM models in a single 3D rendering.

3.2.3.2. Electromagnetic surveys

A frequency-domain, ground electromagnetic survey was conducted over the field area on June 25th and 26th, 2020.

Electromagnetic geophysical techniques are based on the following principle: a primary electromagnetic field (H_p) induces an alternating current in conductive subsurface bodies (Figure 12), which in turn generates a secondary electromagnetic field (H_s) that is a contrary direction to the primary field. The primary current is induced by an alternating current in a transmitter coil on the instrument, and the resultant electromagnetic field is measured by a receiver coil is a combination of the primary and secondary fields ($H_r = H_p + H_s$). Data analysis considers the difference between the primary and secondary currents in terms of delay (time domain) or frequency (frequency domain). In frequency domain instruments, the ratio of the induced secondary magnetic field to the primary magnetic field is directly proportional to the ground's bulk or apparent conductivity. The shape of the transmitted signal can be varied, enabling heightened characterization of a body's size and conductivity.

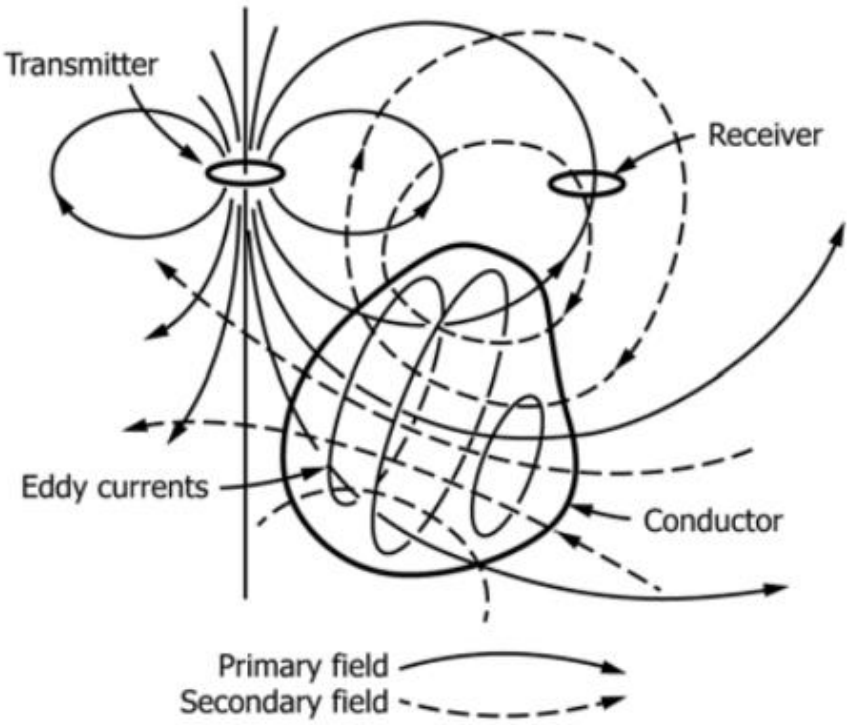

Figure 12. Principles of electromagnetic induction (Sheriff, 1989). Vertical dipole (horizontal loop) configuration is shown.

Common frequency-domain electromagnetic instruments typically operate under the "low induction number approximation," which is a function of the separation between transmitter and receiver, the electrical permeability and conductivity of the ground, and the frequency of the transmitter signal. In the absence of metallic objects in the subsurface, the ratio of the magnitude of the secondary magnetic field to the primary magnetic field (H_s/H_p) is directly converted to an apparent conductivity (σ_a) measurement of earth material (Eq. 1). Outside of the approximation (e.g., where the apparent conductivity > 50 mS/m; Weymer, 2016), the direct correlation of signal response to σ_a breaks down and there is a departure of measured σ_a from "true conductivity," σ. The depth of site characterization is related to the frequency of the alternating current, the distance between the transmitter and receiver coils (intercoil spacing) and coil orientation.

$$\sigma_a = \left(\frac{4}{\omega * \mu_0 * s^2}\right) * \left(\frac{H_s}{H_p}\right)$$

where

σa = apparent conductivity in Siemens/metre (S/m)

ω = 2πf in radians/sec; f = frequency in hertz (Hz)

μ0 = the permeability of free space ($4\pi \times 10^{-7}$ Henry/m; H/m)

s = intercoil spacing in metres (m)

H_s = out-of-phase (quadrature) component of the secondary magnetic field, both measured by the receiver coil;

H_p = out-of-phase (quadrature) component of the primary magnetic field, both measured by the receiver coil;

Instruments usually measure two components of the secondary magnetic field: a component in-phase with the primary field and a component 90° out-of-phase with the primary field (the quadrature component). When ground conditions are such that the low induction number approximation is valid, the in-phase component is dwarfed by the quadrature phase component. If there is a large in-phase response, then the approximation is not valid and there is likely a very conductive body or layer in the subsurface. Specific earth materials can have a large variation in conductivity, which is related to temperature, particle size, porosity, pore fluid saturation, and pore fluid conductivity. Permafrost has low conductivity typically below 1 milliSiemens/metre (mS/m). Importantly, frequency-domain instruments are best used under relatively high electrical conductivity conditions (>1 mS/m). For values less than this, i.e., those most commonly recorded for permafrost samples, better results are obtained with DC resistivity methods (Figure 13).

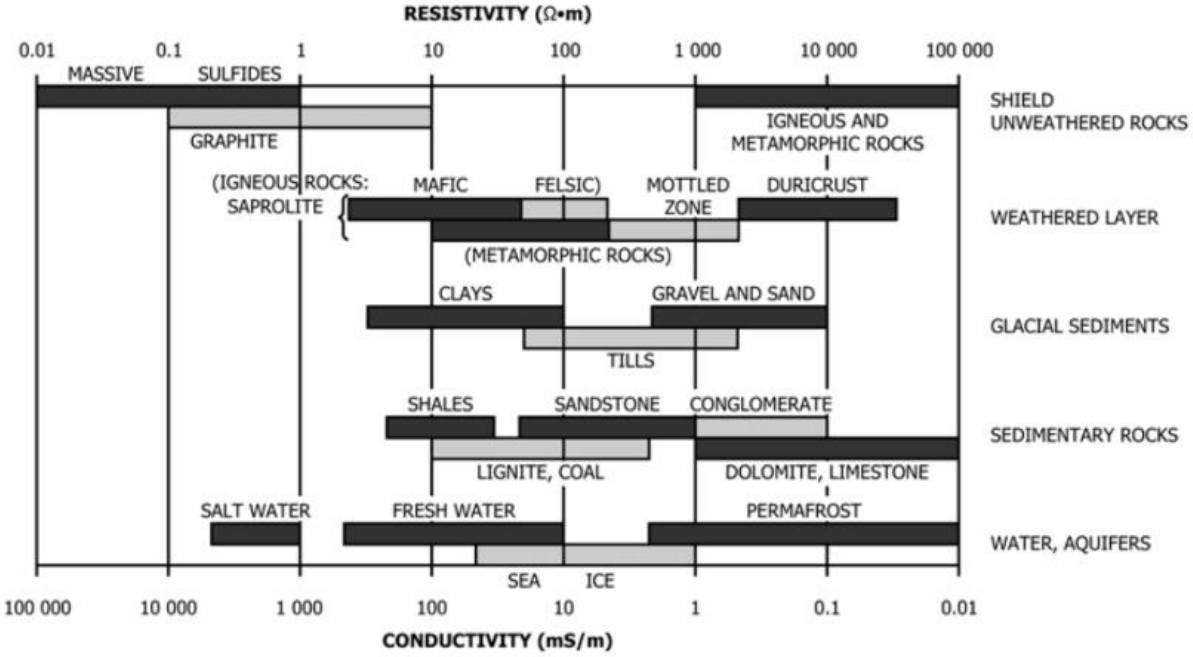

Figure 13. Conductivity ranges for common Earth materials (Sheriff, 1991)

This survey utilized a Profiler EMP-400 survey instrument manufactured by Geophysical Survey Systems, Inc. (GSSI). The EMP-400 is a single user instrument with an inline, 1.29 m (4 ft.) fixed coil spacing. Data was collected at 6 separate frequencies (1, 4, 7, 10, 13, 16 kHz); a low-carry handle was used to maintain a deployment height of ~6 inches (15 cm) above the ground surface.

The data were collected along the 40 x 40 m grid that was laid out over the study area, where each node was a measurement point. Data were collected on two successive days (frequencies 10, 13, and 16 kHz on Day 1; frequencies 1, 4, and kHz on Day 2). There was no precipitation between the two surveys at the study site and temperatures were stable; no significant changes in subsurface conditions (e.g., ground saturation) should have occurred between the two data collection sessions. The two sessions were necessitated by battery life on the instrument and handheld Trimble unit. A stacking value of 8 was used at all nodes, i.e., eight individual readings were averaged at each collection point. A 60 Hz filter was applied during data collection.

Data are presented as six depth slices corresponding to the six frequencies. Gridding was performed using an inverse distance weighted gridding algorithm. Higher frequency data represent shallower depths, while lower frequencies have greater depth penetration. Absolute depth determination is difficult without additional intercoil spacings and/or a change to a horizontal dipole configuration, however, fixed coil

systems typically have depth of investigation (DOI) limits of 6 m. Depth of investigation is strongly influenced by the geological materials underfoot.

3.3. Geospatial analyses

A variety of geospatial analyses were carried out to characterize the site location. These analyses include UAV data to quantify changes in slump morphology, and benchmark surveys to quantify small movements and discern error in geospatial data. Additionally, historical aerial and satellite imagery were analyzed to better understand the morphological history of the site.

3.3.1. UAV image collection and processing methodology

The thaw slump located at km 1456 on the Alaska Highway has been regularly surveyed with UAVs (drones) for aerial image collection since August 2019.

3.3.1.1. Data collection

The surveys have been completed using two models of drones, the DJI Phantom 4 Pro V2 and the DJI Matrice RTK 210. The Phantom 4 Pro V2 is equipped with a camera producing 20MP images. When using this model, eight targets were placed on the ground with their position geolocated using a differential global positioning system (DGPS). The target's locations were used as ground control points (GCP) to produce centimetre-scale positional accuracy for the image processing outcome products.

The Matrice 210 RTK caries a Zenmuse x7 (35mm) producing 24MP images. The RTK system of this drone offers a centimetre-scale positional accuracy not requiring the use of targets.

Mapping grids of various size (all covering the active slump area) were used with 2 different flight altitudes, as indicated in Table 3.

Table 3. Flight mission specifications

Dates	Drones	Mapping grid size	Flight altitude
22-08-2019	Phantom 4 Pro V2	81x67m	60m
11-09-2019	Phantom 4 Pro V2	205x181m	100m
25-09-2019	Phantom 4 Pro V2	527x194m	100m
20-05-2020	Phantom 4 Pro V2	529x194m	100m
11-06-2020	Phantom 4 Pro V2	529x194m	100m
13-07-2020	Phantom 4 Pro V2	237x194m	100m
26-08-2020	Matrice 210 RTK, Zenmuse x7	347x193m	100m
29-09-2020	Matrice 210 RTK, Zenmuse x7	347x193m	100m

3.3.1.2. Image processing

Images were processed using Agisoft Metashape Professional photogrammetry software. For each survey, a point cloud, a 3D model including mesh mapping and texture, a digital surface model (DSM), and an orthomosaic were produced. All final products were projected using UTM zone 8.

Orthomosaics were used to digitize the headwall of the thaw slump with ArcGIS to measure the progression of the slump and its distance from the road at each acquisition date.

3.3.2. Benchmark survey

To quantify small ground movements in the slump area, as well as quantify the error in the differential GPS measurements, a benchmark survey was conducted. This survey included creating 36 rebar benchmarks (Figure 14) that would be surveyed multiple times throughout the field season (beginning in May 2019) using a Trimble R8s differential GPS (DGPS) system. The orthogonal dispersion of the DGPS measurement

points (the dispersion in x and y directions) was used to calculate the standard deviation (SD) of measurements in the x and y directions (SDx and SDy). This analysis was performed using the calc_box function from the R package aspace.

Few points move significantly in the x direction, so the mean SD calculated for this direction ($\overline{SDx}$) is considered reliable. However, many points move significantly in the y direction, skewing the mean SD of the y direction ($\overline{SDy}$). Therefore, to resolve the high $\overline{SDy}$, a threshold value above which values of SDy are deemed to be noise was set as $\overline{SDx}$. Benchmarks with SDy≤$\overline{SDx}$ were used to determine $\overline{SDy}$. Benchmarks with SDy slightly greater than this threshold were examined, and shown to have minimal movement, indicating that if a point begins to move, it will exceed the threshold and be excluded from the determination of $\overline{SDy}$. Then, to quantify the movement of each benchmark in metres, the distHaversine function from the geosphere R package was used, which calculates the shortest distance between two points using the haversine (half-versed-sined) method. This function allows for the distance between the most recent measured coordinate and the original measurement to be calculated, thereby tracking movement. This analysis will therefore allow for quantification of small ground movements in the study area, as well as an assessment of error in the DGPS system.

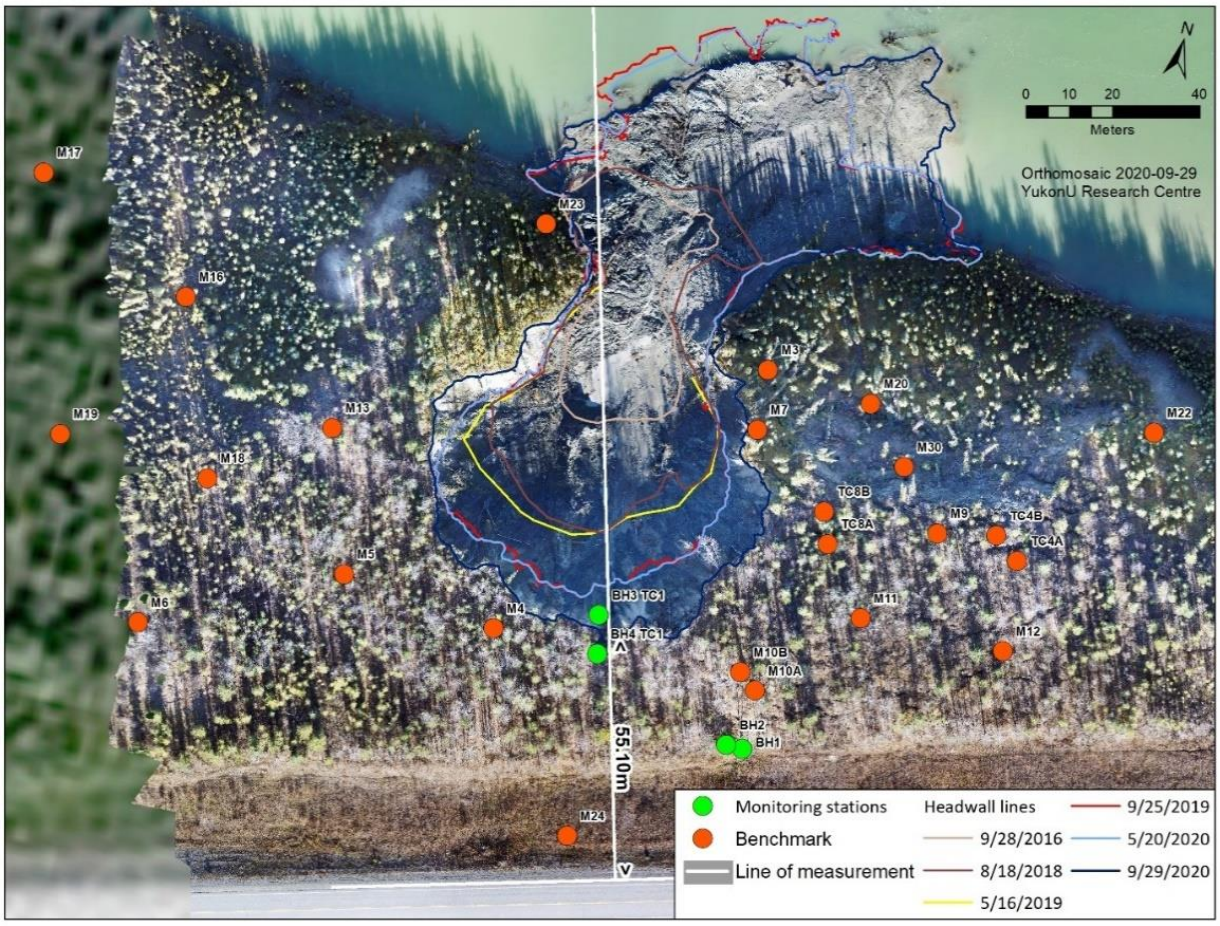

Figure 14. Benchmark survey monuments location and retrogressive thaw slump progression

4. Results

4.1. Geotechnical boreholes

4.1.1. Grain size, ice content and borehole log analysis

The borehole log (shown in Appendix A, No1) for WH_1456_BH1 shows a stratigraphy composed predominantly by clayey silt. The borehole ends at 10 metres in silty sediment (99.9 % silt). Lenticular, micro lenticular, reticulate and suspended cryo-structures (Figure 15) were identified along the profile and the volumetric excess ice content ranged from

13 to 41%. The horizon from 4.5 to 10 metres contained the highest excess ice content. Overall, the borehole has a mean volumetric excess ice content of 32.5% (Table 4).

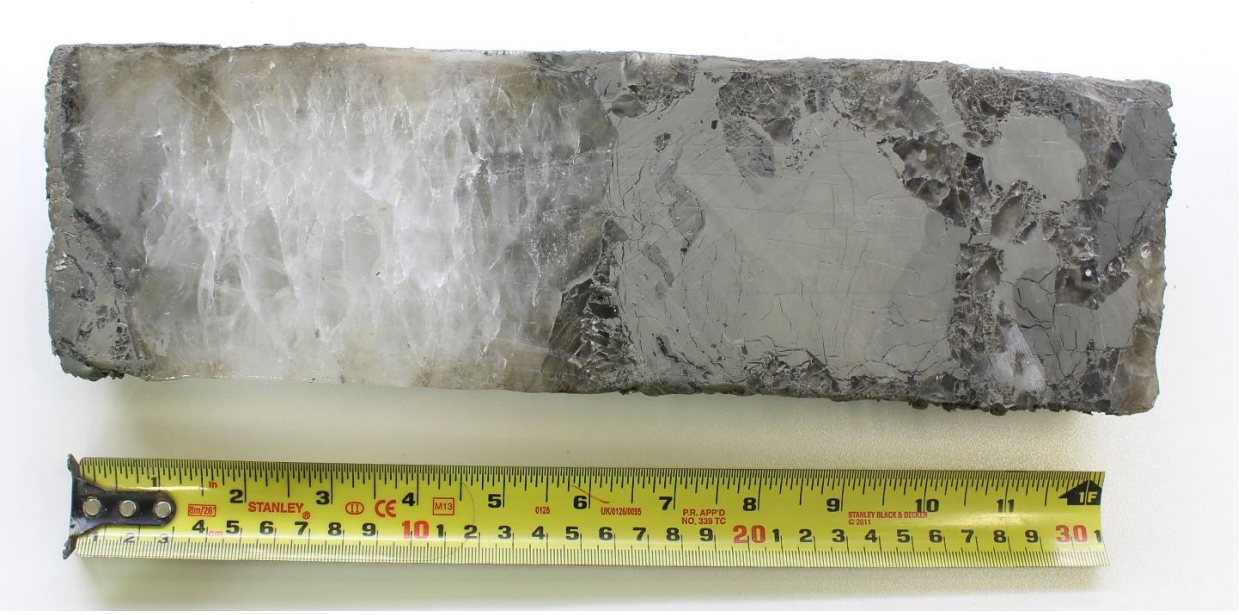

Figure 15. Ice rich permafrost showing thick layered (left) and suspended (right) cryostructures in a core from WH_1456_BH1 at 657 centimetre depth.

Table 4. Geotechnical data. Grain-size and excess ice content results

Sample	Excess Ice %	Cobble %	Gravel %	Sand %	Silt %	Clay %
WH_1456_BH1_0	0.00	0.00	0.04	4.08	72.51	23.38
WH_1456_BH1_152	0.00	0.00	0.09	91.79	7.54	0.58
WH_1456_BH1_304	0.00	0.00	0.00	5.48	79.81	14.71
WH_1456_BH1_335	14.09	0.12	0.00	2.67	78.65	18.56
WH_1456_BH1_457	30.66	0.00	0.00	2.94	83.57	13.49
WH_1456_BH1_480	34.64	0.00	0.00	8.03	81.66	10.31
WH_1456_BH1_563	35.78	0.00	0.00	0.21	90.28	9.51
WH_1456_BH1_596	36.24	0.00	0.01	0.58	76.73	22.67
WH_1456_BH1_657	39.22	0.00	0.00	0.38	85.70	13.92
WH_1456_BH1_703	36.39	0.00	0.00	0.08	64.31	35.61
WH_1456_BH1_745	34.62	0.00	0.00	0.16	92.19	7.65
WH_1456_BH1_785	13.36	0.00	0.00	1.20	87.05	11.75
WH_1456_BH1_822	39.50	0.00	0.00	0.01	67.70	32.29
WH_1456_BH1_850	36.59	0.00	0.00	1.70	87.41	10.89
WH_1456_BH1_878	41.63	0.00	0.00	0.06	68.13	31.81
WH_1456_BH1_915	26.34	0.00	0.00	0.12	70.13	29.75
WH_1456_BH1_940	33.88	0.00	0.00	0.15	99.85	0.00

The borehole log for borehole WH_1456_BH3 (BH3) (Appendix A, No2) shows layers of ice rich gray clayey silt alternating with some very ice rich layers. While drilling was initiated in frozen ground, at approximately 2 m depth a thin unfrozen section of soil with the presence of ground water depth was encountered. The borehole extends to six metres with clayey-silt sediment. Lenticular and micro lenticular cryo-structures were identified along the profile (Figure 16).

Figure 16. Ice rich permafrost core showing suspended cryostructure collected from borehole WH_1456_BH03

The grain size distribution of sediments determines the porosity and hydraulic conductivity of the ground. Coarse material (medium sand and coarser) has a high hydraulic conductivity and readily drains water as ice melts, whereas fine-grained material drains poorly once it thaws due to its low hydraulic conductivity. Furthermore, fine-grained sediments often contain excess ice (i.e., the volume of ice in exceedance of the total pore volume of the ground when unfrozen) and may form ice lenses or layers by ice segregation. On flat terrain, ground with excess ice will undergo severe thaw

settlement; likewise, on slopes, silt and clay deposits may experience mass movement when the pore water pressure created by melting ice is high. For slope deposits, the plastic and liquid limits of the material are used to evaluate the potential for ground failure.

The nature of the ground ice is segregated with the dominant cryostructures being suspended and thick layered ice. These types of cryostructures form in ground where the freezing front progresses slowly (low thermal gradient) with a ground water supply sufficient to accommodate the growth of thick ice layers and lenses. Usually, the thickness of the ice layer increases with depth as the freezing plane slows down. This type of cryostratigraphical record is consistent with an epigenetic discontinuous permafrost such as encountered in wet, frost-heave mounds and permafrost plateau environments.

4.1.2. Ground temperature and environmental conditions

Air temperature and precipitation data from the Whitehorse Airport weather station for April 17 to December 31st, 2020 can be seen in Figure 17 below (A and B). Figure 17 C and D shows the ground temperature for boreholes 2 and 3 from the thermistors. Trumpet curves for boreholes 2 and 3 can be seen in Figure 18 below. The trumpet curves in Figure 18 suggest that the top of the permafrost is between 3 metres (BH3) and 4 (BH2) metres, and reaches a depth of 8 m, suggesting that the permafrost is 4-5 m deep (see limitation below). In BH3, the ground is frozen below 3 m to the bottom of the borehole (6 m) for the duration of the recording period (June 5th until the borehole failure on August 12th, 2020).

Overall, the ground temperature data suggest that temperatures below 0 °C do not persist below 8 m of depth. It is possible that this is due to the disturbance caused by the drilling process, which may upset the thermal regime by thawing the permafrost around the borehole. While it is possible that the temperatures will stabilize over time, the disturbance could be permanent. Interpretations of the permafrost boundaries based on ground temperatures in the boreholes should be considered with caution.

A considerable amount of ground water was observed during the drilling process, which could be causing the ground temperatures above the freezing point. We believe that

even if the mean ground temperature is slightly above 0°C, the significant amount of ice present in the ground is preventing permafrost from thawing because of the latent heat (the amount of heat required to melt all the ice in a unit of soil or rock) absorbtion required to change ice to liquid water.

Temperature data from BH 3 (Figure 18B) show that as the headwall retreats towards the borehole, temperatures at 0.5 m and 1 m of depth steadily increase beginning on the 6th of August. A less prominent increase is also seen beginning on August 6th at 3-6 m of depth.

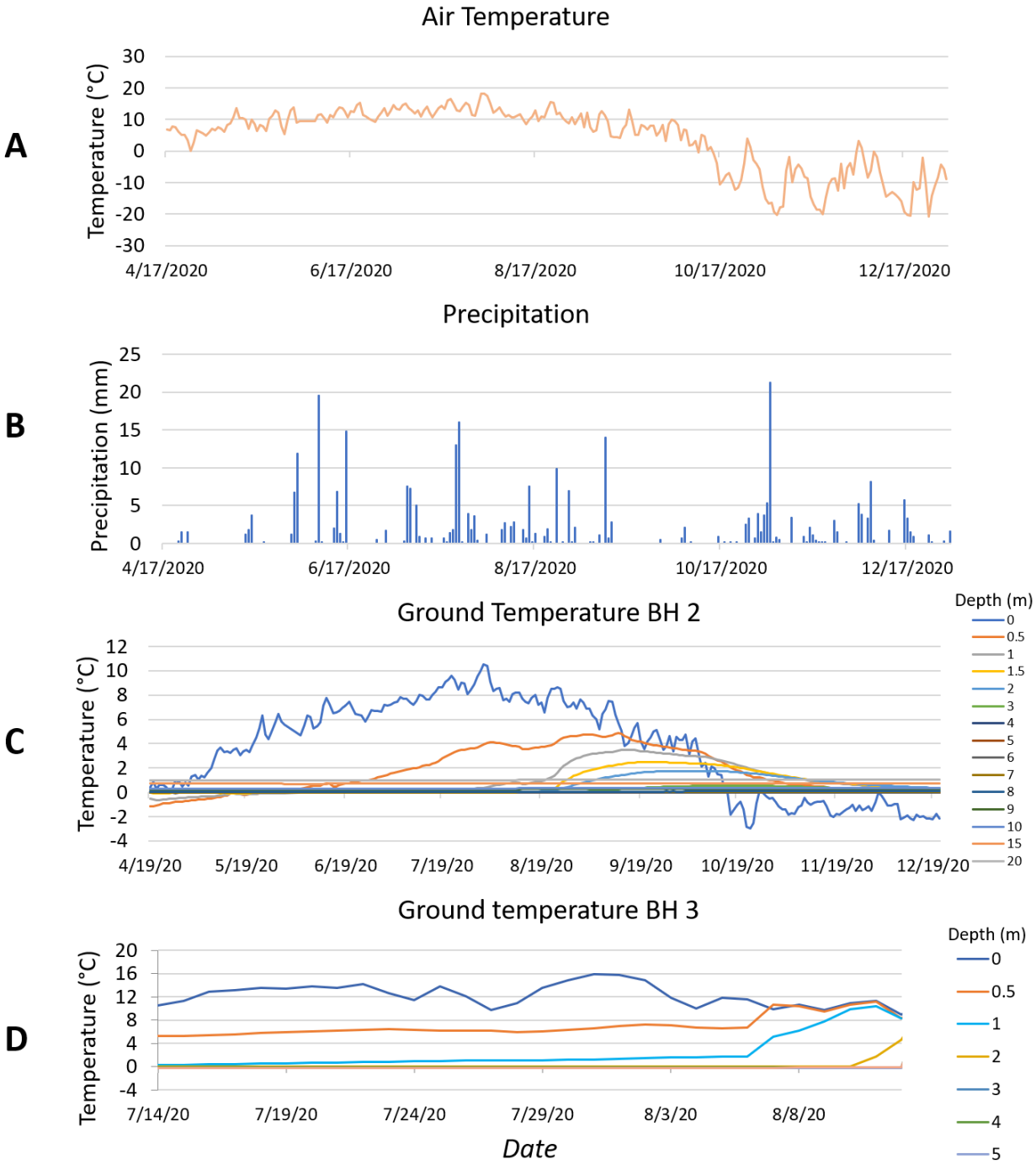

Figure 17. Environmental factors for study site including: A) Air temperature; B) Precipitation; C) Ground temperature for BH2; and D) Ground temperature for BH3 (notice change in x-axis)

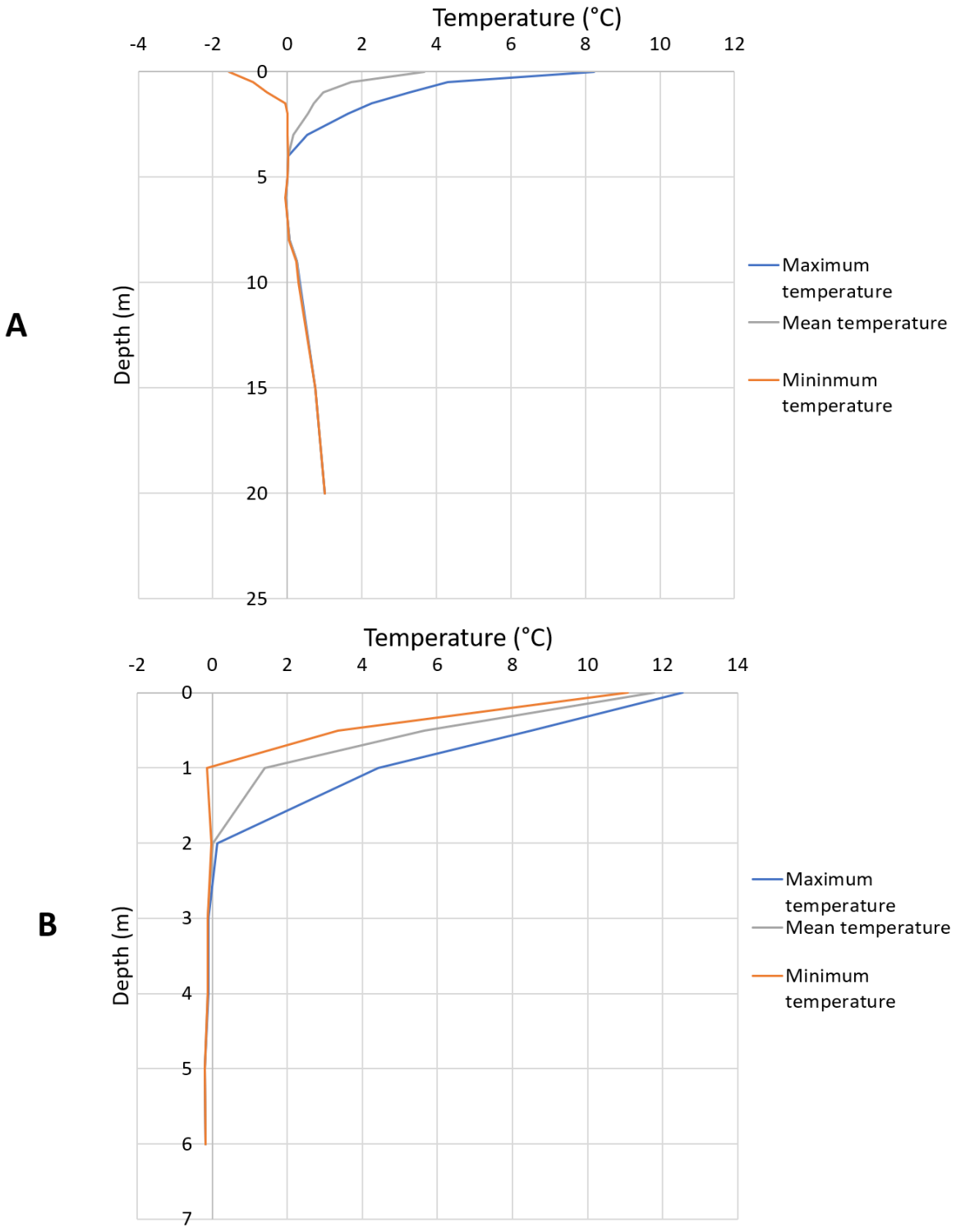

Figure 18. Trumpet curves for A) BH2 using temperature data from April to December, 2020; B) for BH3 using temperature data from June to August, 2020

4.1.3. Soil moisture

Despite the limitations of the soil moisture data from the METER-EC 5 soil moisture sensors in BH3, the normalization of the data allows for an adimensional analysis of trends in soil moisture leading up to the failure of the slump. Figure 19 below shows the variations in the normalized soil moisture from June 2nd until the slump failure on August 12th, 2020. There was little variation in soil moisture for all depths until the beginning of August, showing trends similar to those seen in the temperature data. The greatest increase is seen at depths of 1 m and 5 m on August 6th, though increases are seen at all depths on the same date except for at 2 m, where an increase in soil moisture is seen on August 10th.

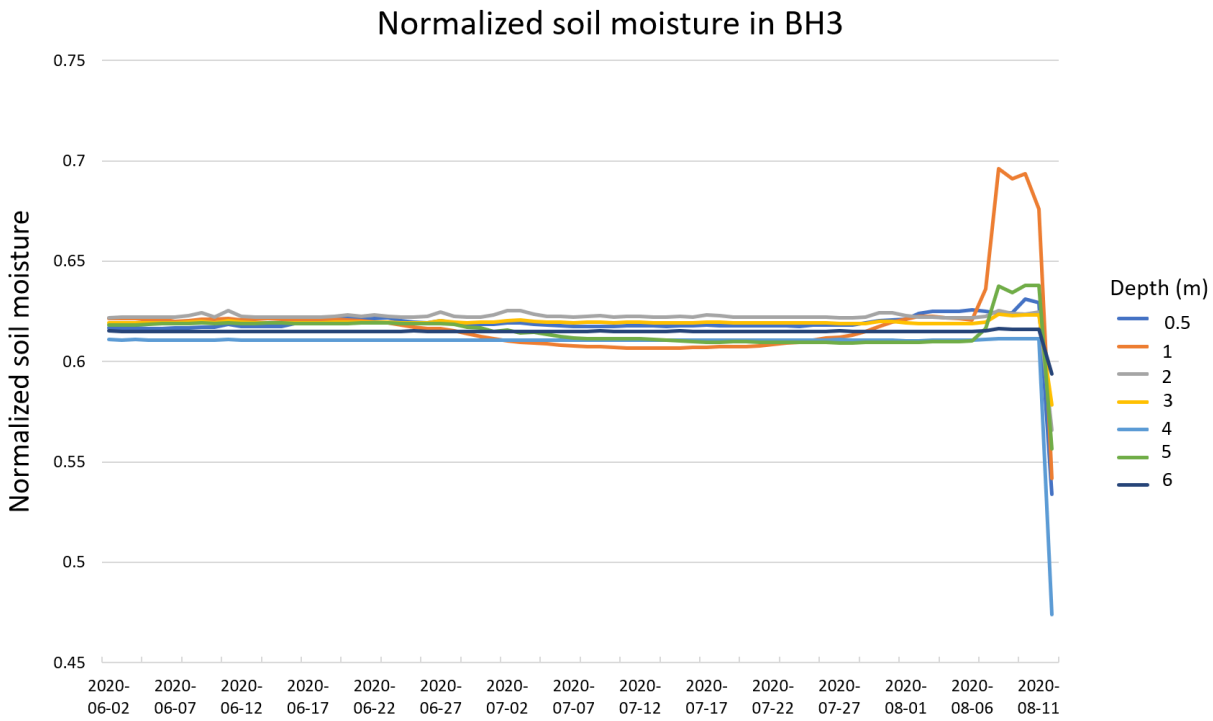

Figure 19 Daily normalized soil moisture in BH3 from June 2nd to August 12th 2020

4.1.4. Inclinometer

The inclinometer data from Measureand's ShapeArrays in Boreholes 2 and 3 provide information on soil deformation and movement in the slump area. Figure 20 and Figure 21 below show the movement of the sensor at multiple depths for Boreholes 2 and 3, respectively. The movement in Borehole 2 is relatively constant with some minor gaps due to missing data or suspected interference during field visits. There is a noticeable movement at the surface that decreases in importance with depth on August 12th at the time of the major headwall retreat event. The August 12th movement is predominantly a downslope one (in the y-direction), of approximately 10 mm (Figure 20). The sensor movements within the borehole are oscillating (backwards and forwards) throughout the recording period. Therefore, the absolute displacement only amounts to 5 mm in the x-direction and 22 mm in the y-direction at the surface (less than the sum of all relative movements) over the entire recording period (April-December, 2020).

In BH3, the movements are much more significant. The array is stable in BH3 until a movement is initiated on August 6th by 200 mm in the x and y directions, followed by another 200 mm movement (predominantly in the y-direction) (Figure 21). A final 600 mm movement in the y direction (downslope) on August 12th represents the borehole failing due to the retreat of the slump headwall (Figure 21). The absolute displacement amounts to 237 mm in the x-direction and 1160 mm in the y-direction at the surface (less than the sum of all relative movements).

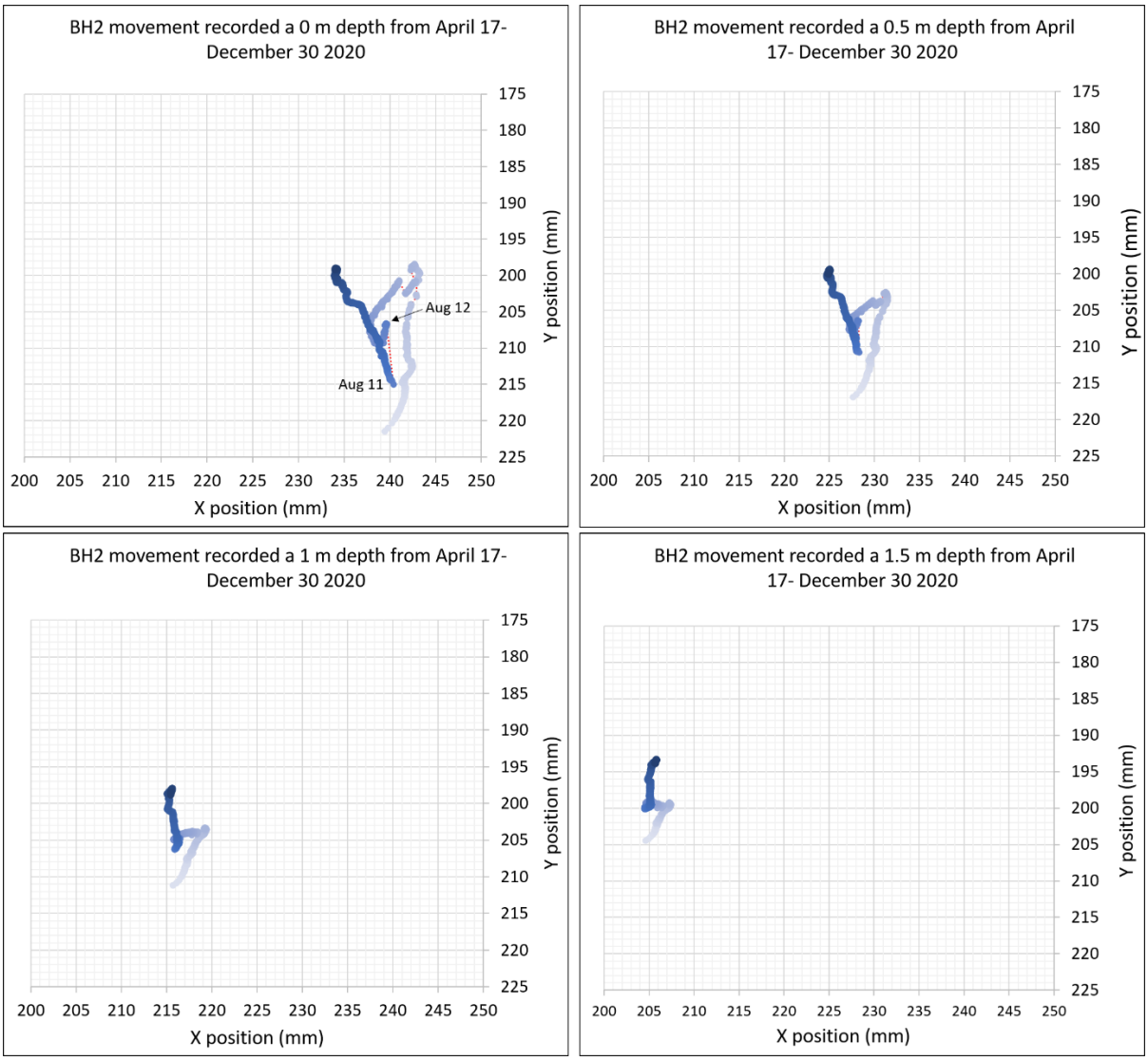

Figure 20. Cumulative deviation from initial position on April 17th to final recording on December 30th, 2020 in BH2 for 0, 0.5, 1 and 1.5 m depth

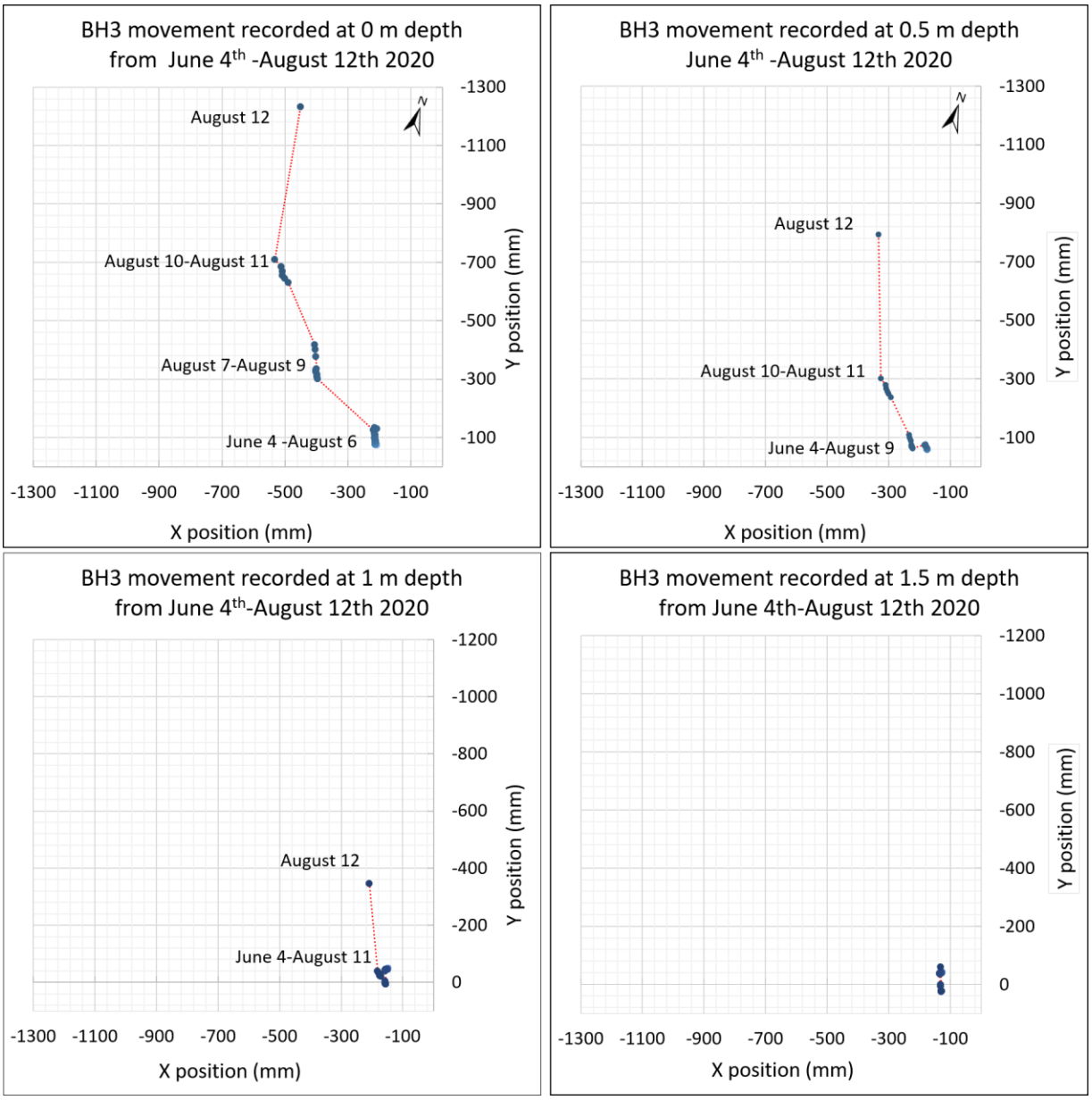

Figure 21. Cumulative deviation from initial position on June 4th to final recording on August 12th, 2020 in BH3 for 0, 0.5, 1 and 1.5 m depth

The inclinometer data provides a clear picture of ground movement close to the slump in BH3. The data recorded in BH3 from June until the borehole failure on August 12 provides a unique window into the failure processes occurring in the slump. The trends of the movements at multiple depths are extracted from this record and give an understanding of the mechanics leading to the failure. The daily change between positions was computed and is shown in Figure 22 for depths up to 1.5 m where the most important movement occurred. This change in daily slopes shows trends similar to

those of the ground temperature data (Section 3.1.3), with little movement up until the 6th of August, at which point there is increased movement leading up to the slumping event. This trend is also seen if the change in position is downscaled to three-day movements (Figure 23).

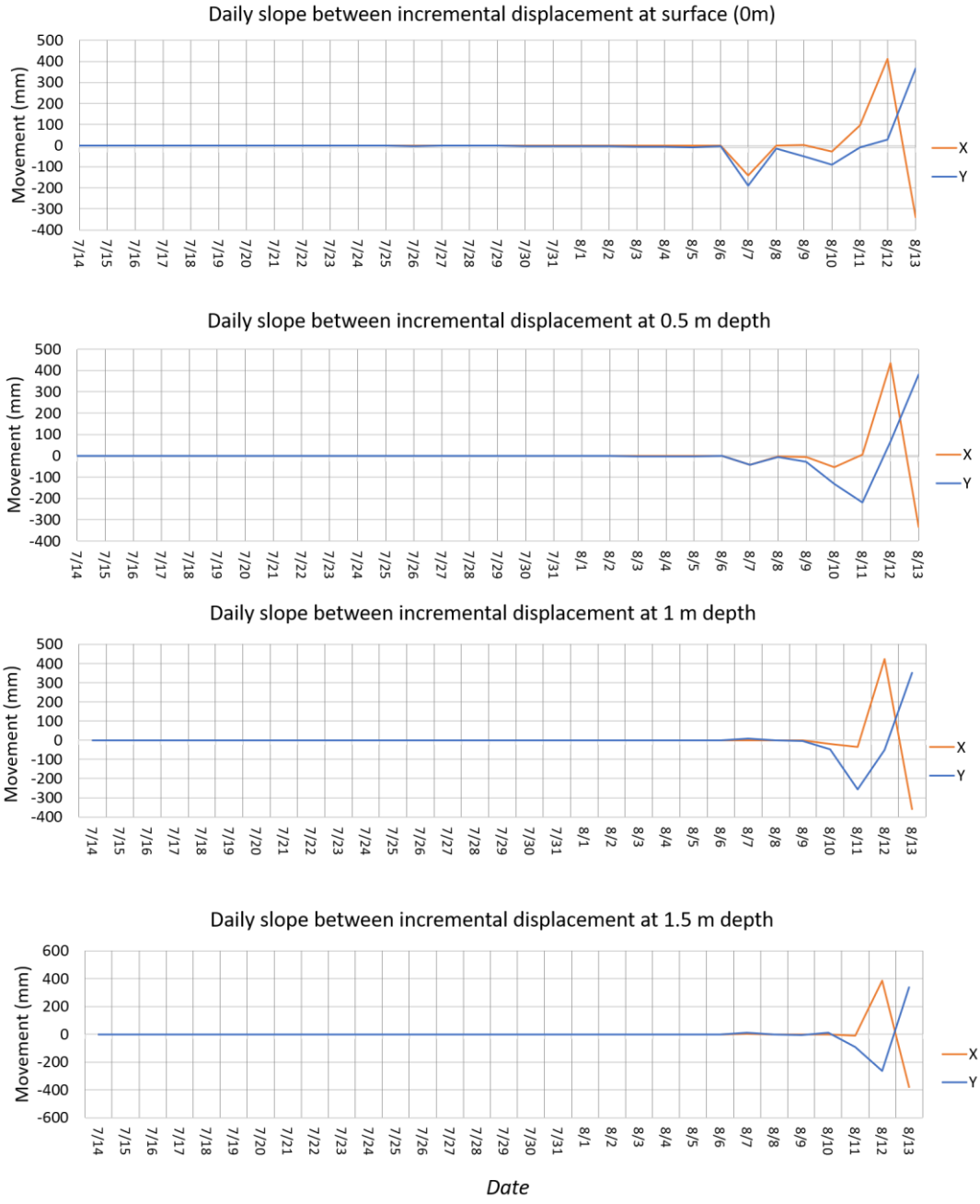

Figure 22. Daily change in position (slope) for surface; 0.5 m depth; 1 m depth; and 1.5 m depth between July 14th and August 12th in BH3

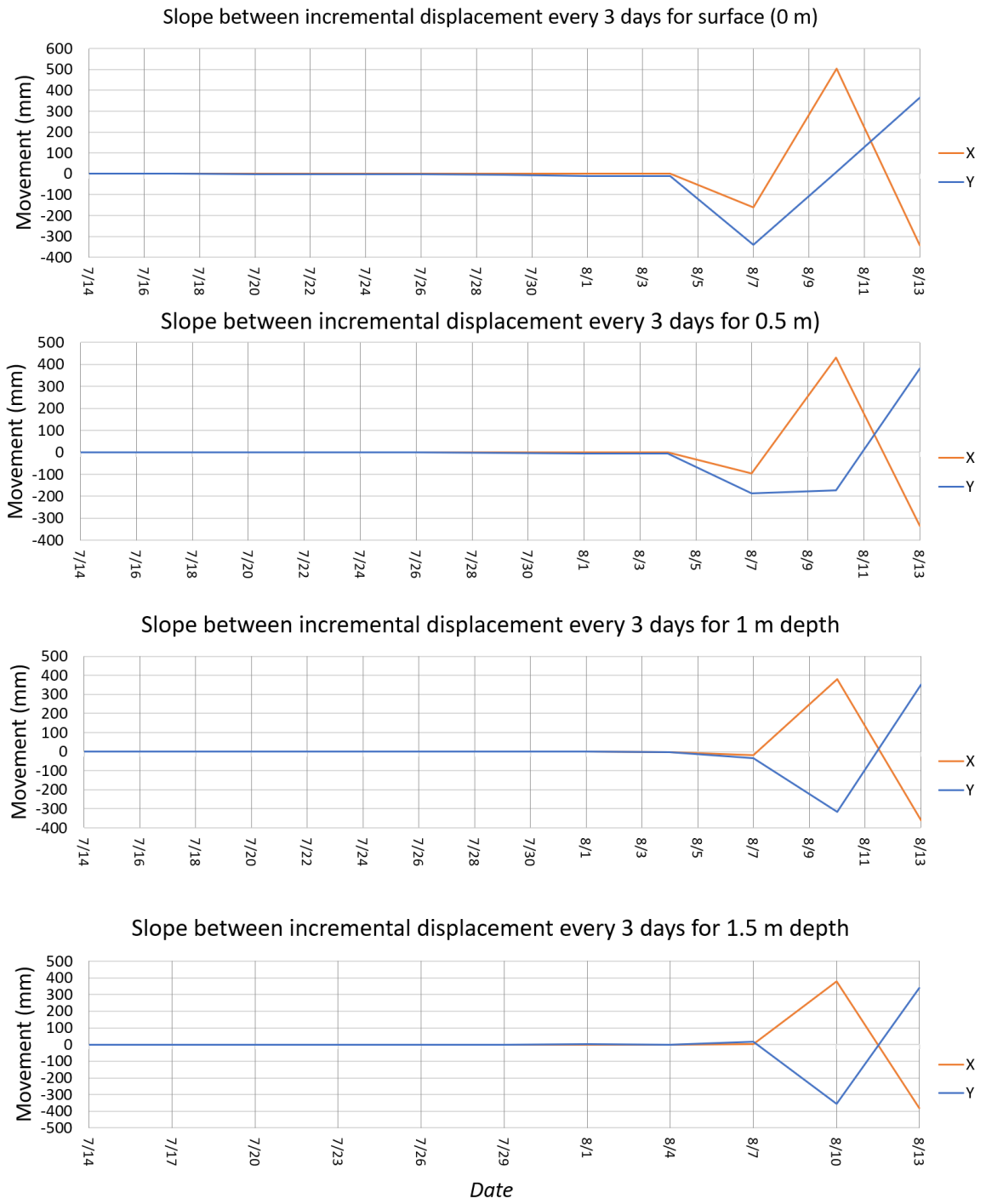

Figure 23. Change in position (slope) every 3 days for surface; 0.5 m depth; 1 m depth; and 1.5 m depth between June 5th and August 12th in BH2

These trends can also be visualized in the velocity of the movements, as shown in Figure 24. This figure shows relatively stable velocities of less than 1 mm/6 hour period at various depths until the end of July (surface) or beginning of August (0.5 m, 1 m and 1.5 m depths). Towards the end of July and beginning of August, there is a steady increase in movements until the slumping event on August 12th.

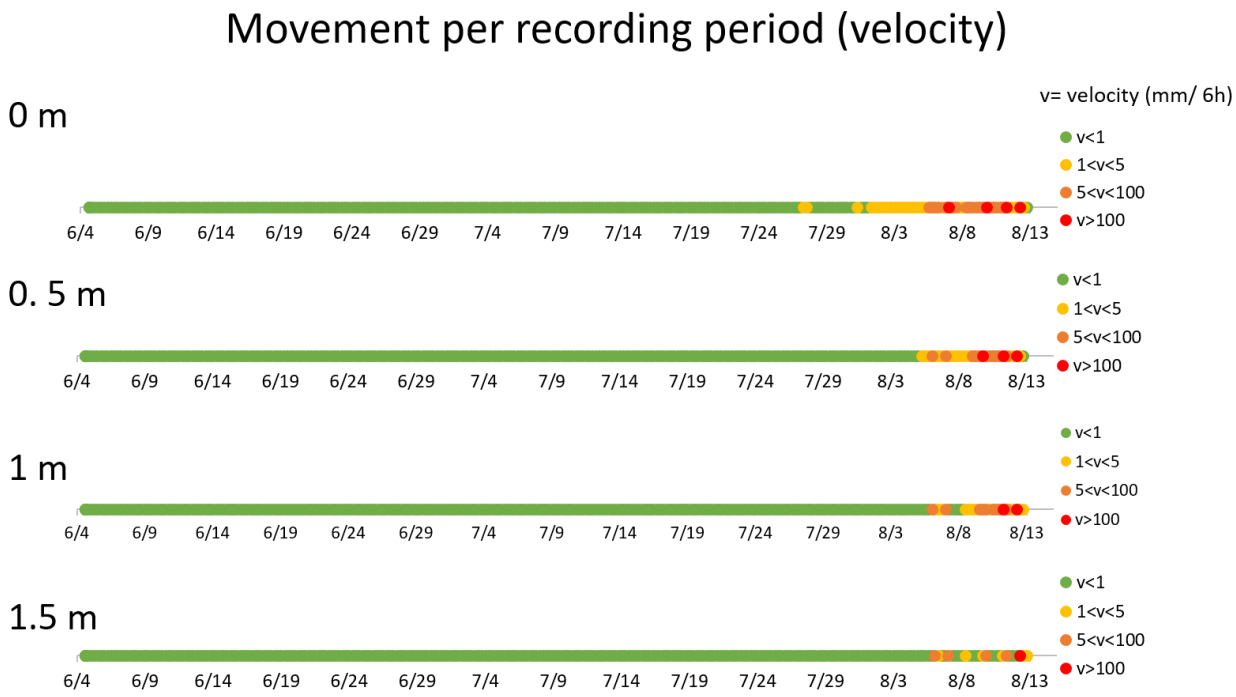

Figure 24. Velocities of combined x and y movement per recording period (mm/6h), where v is the velocity for A) the surface (0 m); B) 0.5 m depth; C) 1 m depth; D) 1.5 m depth

4.2. ERT and EM

4.2.1. ERT

Four ERT surveys were conducted on this site (Table 2). For two of these surveys (WH_1456_ERT1 and WH_1456_ERT2) both the Wenner and dipole-dipole array configuration were measured. For WH_1456_ERT3 and WH_1456_ERT4 only the Dipole-dipole array was measured. The results obtained with the Wenner and dipole-dipole arrays mostly show similar resistivity distributions in the ground, however the dipole-dipole array shows more detail relative to the low resistivity areas.

The WH_1456_ERT1 survey was completed on June 14th, 2019. It ran from east to west, through a dense undisturbed deciduous mixed forest (Figure 25) 12 metres away from the headwall. Data suggests that permafrost could be as deep as 30 metres towards the eastern part of the survey. High resistivity pockets (dark blue shades) seem to be concentrated between 25 to 50 metres along the survey. Some tension cracks manifested at the ground surface.

The permafrost table could be at its shallowest towards the western end of the profile, where the resistivity values remain relatively high (2500 ohm.m). A lower resistivity core (red shades) can also be observed at 40 metres; this could potentially be the result of a ghosting effect from the high resistivity material above or associated with water movement. Another lower resistivity core can be observed at 180 metres from 8 to 12 metres depth. This could be the result of underground water flow within the permafrost, due to the discontinuous distribution of permafrost in the Takhini Valley.

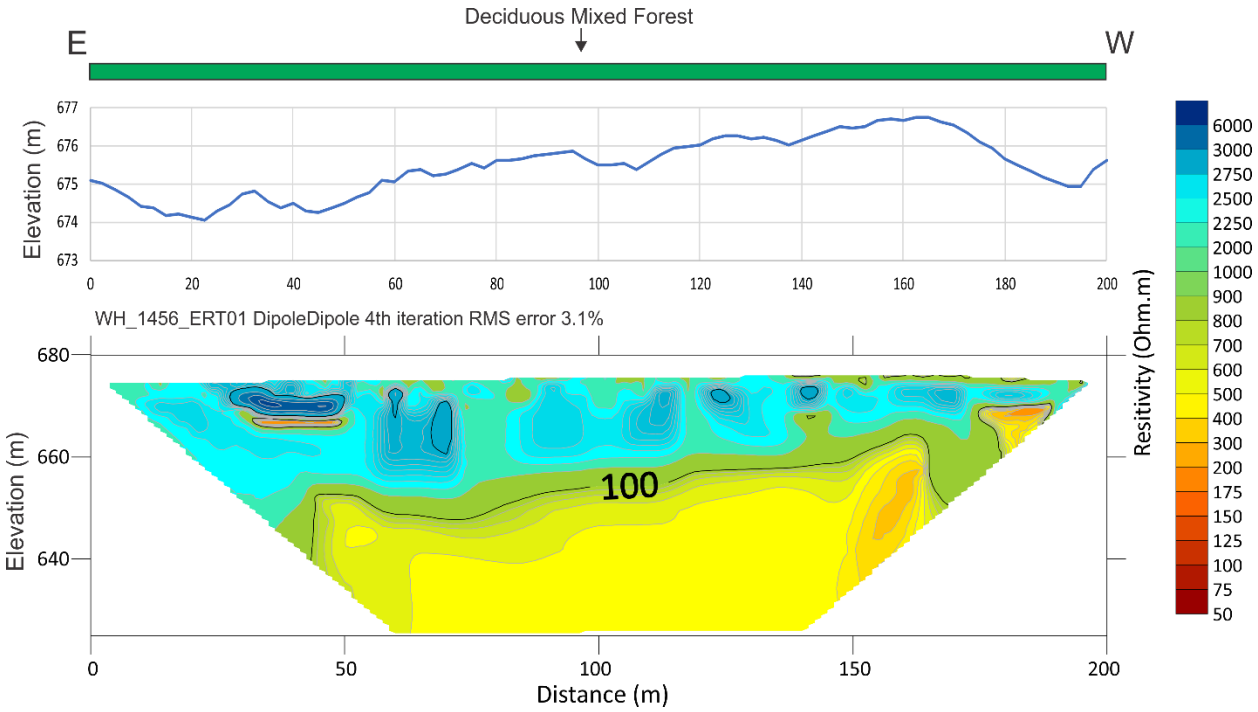

Figure 25. WH_1456_ERT1 Dipole-Dipole 200 metre transect (east to west)

WH_1456_ERT2 was conducted on July 16th, 2019. This transect ran east to west (Figure 26) in a deciduous mixed forest, along the cleared portion of the right of way of the Alaska Highway and 30 metres away from the headwall. The survey intercepted the

borehole location of WH_1456_BH2 at electrode 31 and WH_1456_BH1 at electrode 32. The vegetation cover was colonized predominantly by trembling aspen, and white spruce. The underbrush, composed mainly of small aspen, willow and soapberry, was dense in the first and last quarter of the profile. It then became more open between 60 and 80 metres. The survey intercepted metre-deep tension cracks at 5 and 135 metres along the profile (Figure 26).

The resistivity data suggests that the permafrost is more discontinuous closer to the highway. High resistivity pockets (blue shades) are concentrated between 50 and 80 metres. This cluster of high resistivity, which likely represents ice rich permafrost, could also be observed on WH_1456_ERT1. Permafrost distribution seems more localized and does not tend to go deeper than 20 metres at its deepest t (77.5 metres along the profile). Some small high resistive pockets (light blue) can be observed at 30, 115 and 180 metres. Low resistivity areas (red/orange shades), at 35 and from 115 to 200 metres may indicate ice poor and/or unfrozen material, or the presence of liquid ground water circulating within permafrost. It is not impossible to have permafrost in areas with resistivity as low as 100 ohm.m, because in fine-grained materials, near-0°C temperatures can result in higher liquid water content resulting in low resistivity values.

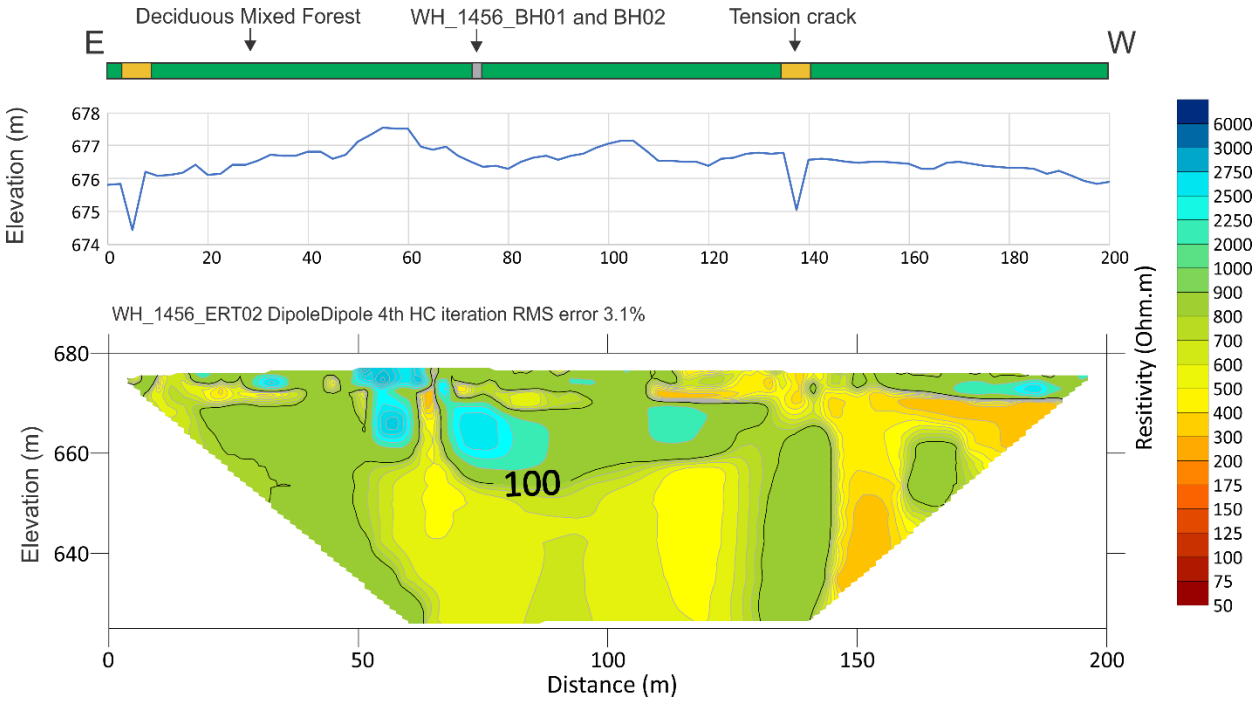

Figure 26. WH_1456_ERT2 Dipole-Dipole 200 metre transect (east to west)

WH_1456_ERT3 was completed on August 23rd, 2019. The 500-metre survey ran west-east (Figure 27) along the right-hand side of the Alaska Highway embankment, going down a gentle slope. The vegetation cover was open and colonized predominantly by small trembling aspen, willow, and some spruce saplings. The data suggests localized high resistivity areas (dark blue) up to 7 metres deep from 20 to 110 metres along the profile. Material from 200 to 280 metres along the survey is likely to be unfrozen. Some deep low resistivity pockets (red shades) visible at 265 and 365 metres could be associated with groundwater flow.

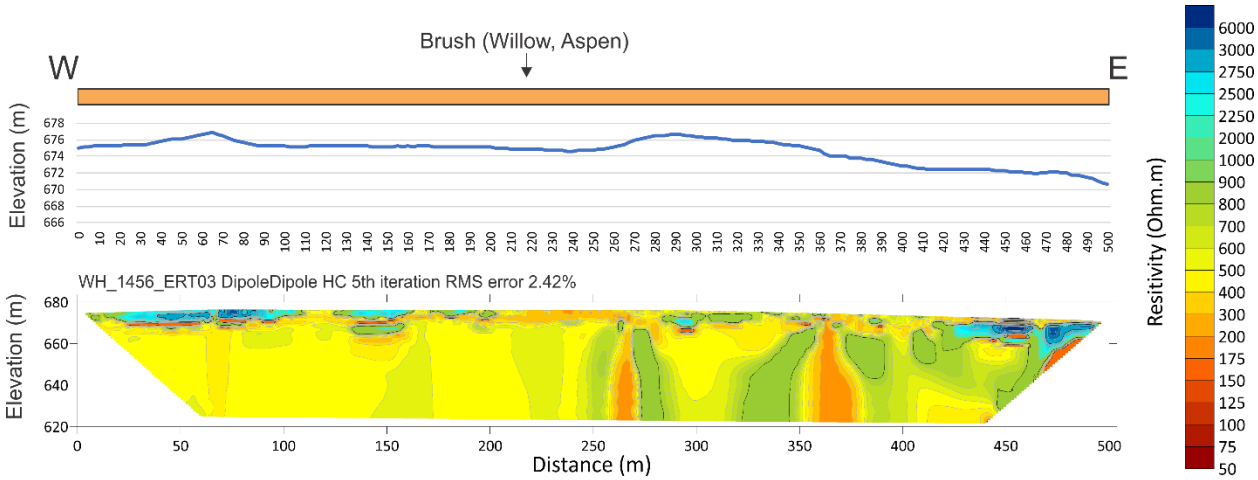

Figure 27. WH_1456_ERT3 Dipole-Dipole 500 metre transect (west to east)

WH_1456_ERT4 was completed on September 12th, 2019. The 500-metre survey ran west-east (Figure 28) along the left-hand side of the Alaska Highway embankment, going down a gentle slope. The vegetation cover was very similar to the one encountered at WH_1456_ERT3, which included small trembling aspen, willow, and some spruce saplings. The data shows high resistivity areas (blue shades) down to 7 metres deep, along most of the profile. Only the first 70 metres of the survey seem unfrozen. One larger highly resistive cluster, towards the end of the profile (450 to 500 metres) show potential ice-rich material from 17 to 35 metres of depth. Some shallow low resistivity pockets, between 5 and 10 metres of depth along the profile could be associated with groundwater flow within permafrost.

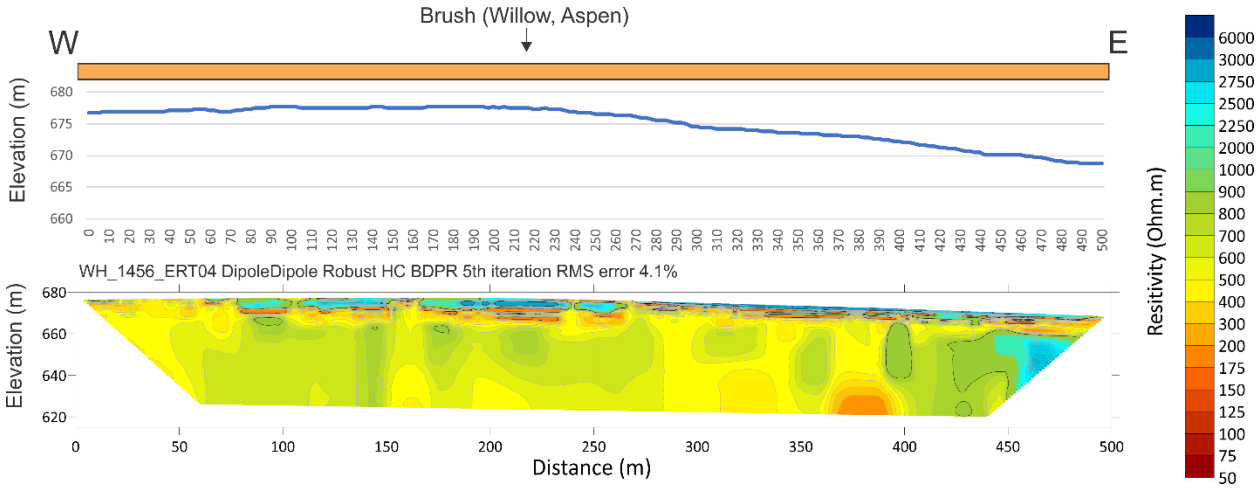

Figure 28. WH_1456_ERT4 Dipole-Dipole 500 metre transect (west to east)

Overall, the very high-resistivity areas (dark blue) are attributable to ice-rich fine-grained sediment (clayey-silts); they increase as you get closer to the headwall and become more sporadic closer to the highway. The low resistivity values could be attributable to ice poor and/or unfrozen material, the lowest values may indicate the presence of liquid ground water.

4.2.2. 3D ERT & EM

The EM and 3D ERT surveys are an experimental attempt to obtain a three-dimensional representation of some of the ground properties, primarily ground ice content and groundwater occurrence. While the processing of the 3D ERT survey did not provide any specific difficulties, that of the EM data did.

The EM data products consist of horizontal slices representing ground conductivity for each investigated frequency (1, 3, 7, 10, 13, and 16 kHz). The preliminary results presented in this section remain tentative as EM data require additional post-treatment, specifically regarding the calculation of the skin depths, i.e. the depths of investigation for each surveyed frequency. The skin depth δ is given by the following equation:

$$\delta = \sqrt{\frac{2}{\omega\mu\sigma}}$$

Where $\omega = 2\pi f$ and f is the frequency in Hz

$\mu = 4\ \pi.\ 10^{-7}$ (magnetic permeability)

σ= electrical conductivity in of the geologic materials of interest in S/m

In the case of the present survey, the equation is especially difficult to solve because the result is influenced by the nature of the investigated soil, which in this case is a non-homogenous/isotropic geologic medium consisting of a sedimentary soil that can be either dry and/or wet with a variable content of ground ice along the profile. To circumvent this difficulty and proceed with a tentative 3D model, a depth of investigation was attributed to each EM slice based on an empirical approach. The approach relies on two hypotheses: 1- the equation suggests that a linear relationship should exist between depth and frequency and could be used to locate the slices; 2- the manufacturer of GSSI Profiler EMP-400 system suggest that the depth of investigation of its system is limited to about 7.5 m.

Consequently, boundary depths of 0 m and 7.5 m have been attributed to 16 kHz and 1 kHz frequencies, respectively, while the other frequencies were linearly spread along the 10 m depth interval.

The EM and ERT survey slices are presented in Figure 29. The EM survey shows constant pattern across each frequency: conductive material (red hues) located in the south border of the slices; a large low conductivity area (blue hues) at the east and a smaller low conductivity area at the west. The ERT slices show the same type of pattern where resistive material (blues) are present at the east and at the west, and low resistive material (reds) are present at the south. In addition, the resistivity of the ground increase progressively with depth. Those observations are consistent with drillings and 2D ERT observations. The reddish areas are located near the road where vegetation was cleared, the soil is wet and less likely to be frozen. The blue areas likely represent areas of ice-rich ground.

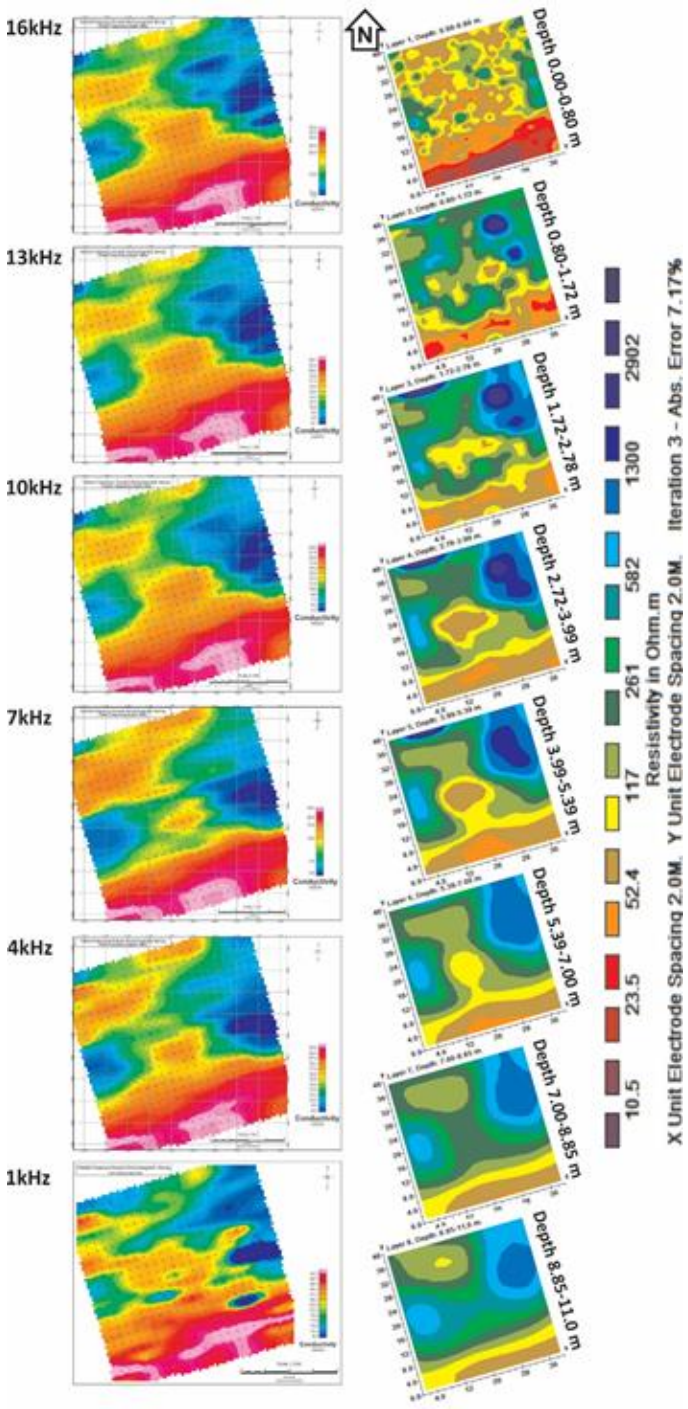

Figure 29. EM (left) and ERT (right) surveys horizontal slices, from shallower slices of the top to deeper slices at the bottom. The slump is located northward, and the road southward

Figure 30 shows a 3D representation of the EM survey. This representation shows the warmer area along the southern edge of the survey, which is cleared and runs along the road. It also shows the two ice-rich bodies closer to the slump. Figure 29 shows a

comparison between EM and ERT data; for this representation, only the high-resistivity bodies are shown as discreet blue volumes (delimited by the dotted line in Figure 31). Overall, there is a strong relationship between the two types of geophysical data.

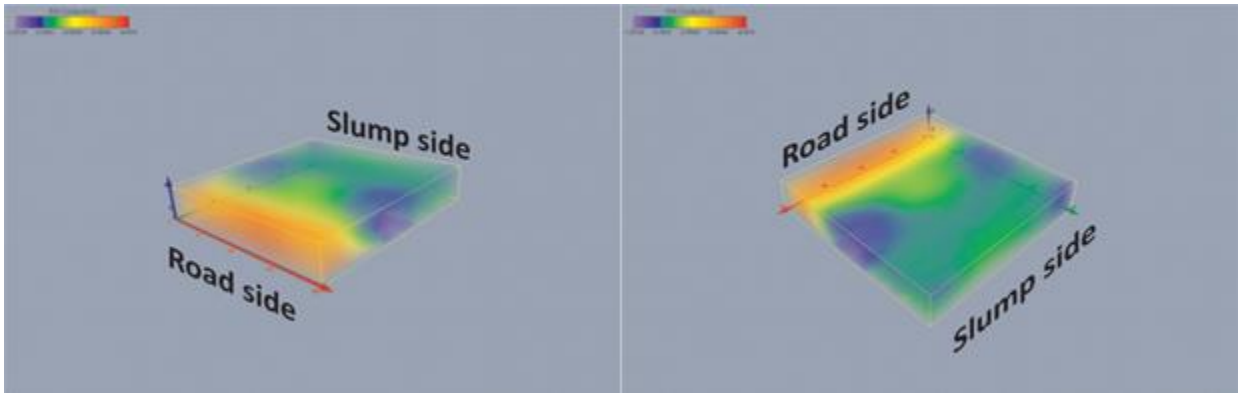

Figure 30. EM survey at km 1456 of the Alaska Highway. The blue areas show ice-rich permafrost zones while the red areas show warm or thaw permafrost zones

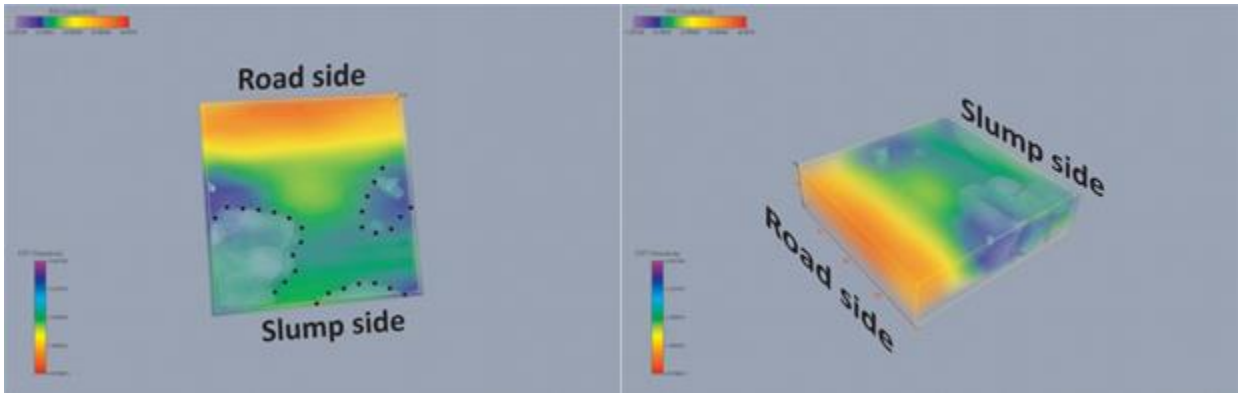

Figure 31. Comparison between EM and ERT surveys at km 1456 of the Alaska Highway. Comparison shows a good correlation between the two types of surveys. Dotted lines indicate ice-rich areas identified by the ERT survey

Observing the 3D ERT model alone, some specific features can be observed when specific iso-curves, which correspond to specific resistivity values, are shown separately. By focusing on high-resistivity values, ice-rich zones can be visualized in the model (blue iso-curve in Figure 32). When looking at intermediate resistivity values, a boundary between firmly frozen ground and wet or unfrozen ground can be implied (green iso-curve in Figure 32). These observations suggest that the ground ice distribution is not

homogenous across the area, but rather that ice-rich ground is present in clusters. The data also suggest the presence of a groundwater channel crossing the site in at south-north direction. This is not surprising as springs have been observed on the headwall as well as in some of the boreholes during drilling.

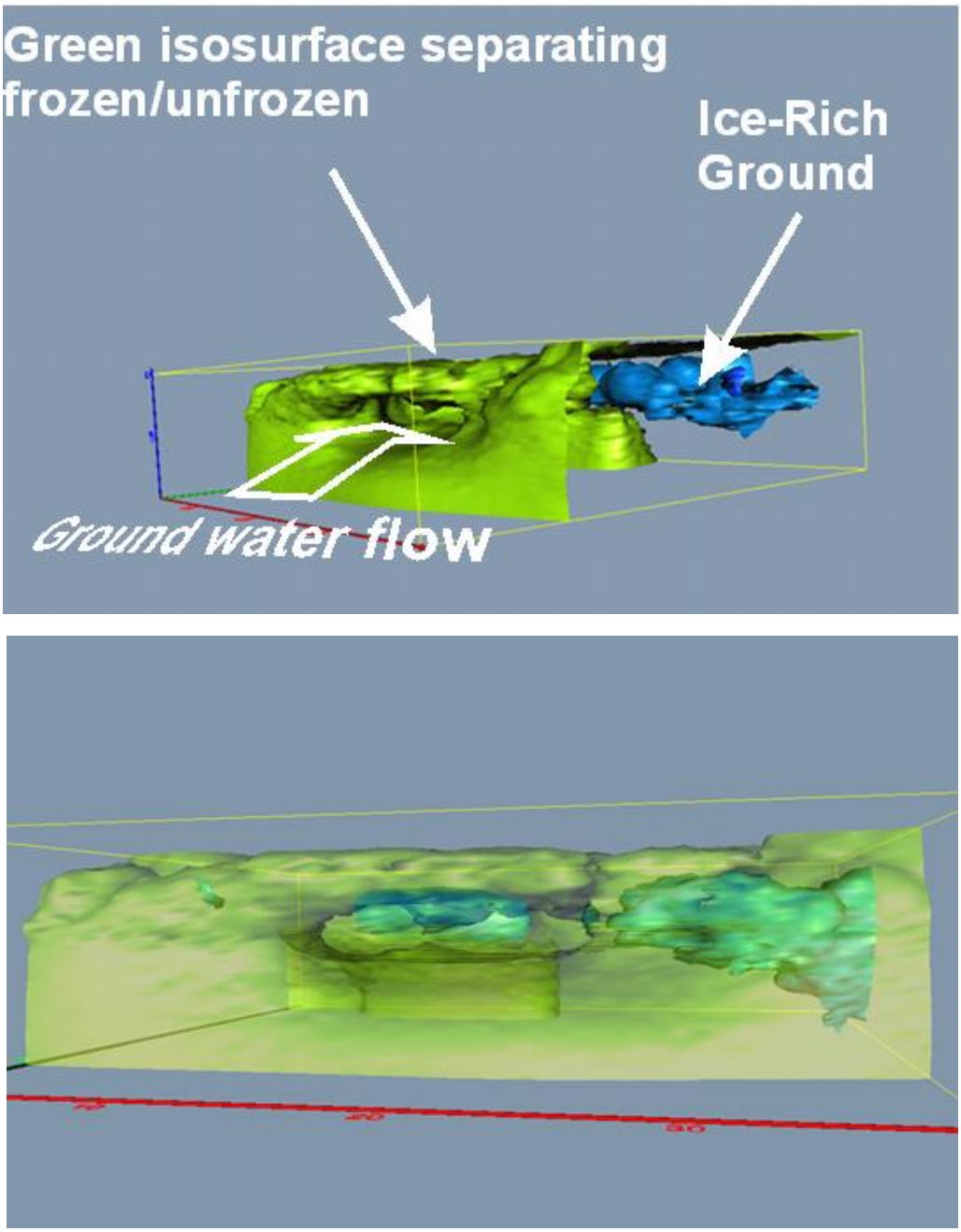

Figure 32. 3D ERT survey at km 1456 of the Alaska Highway. The blue bodies are ice-rich permafrost zones while the greenish iso-curve separate warm and/or wet and/or unfrozen areas from frozen ground

4.3. Geospatial analyses

4.3.1. Field, aerial and satellite imagery, and UAV observations

The UAV surveys allowed for the creation of high-resolution imagery (orthomosaics) and DSMs, with ground sampling distances ranging between 1.14 cm and 2.97 cm for the orthomosaics and between 2.29 cm and 5.94 cm for the DSMs (Table 5). The absolute accuracy of the products is also very high, for example the September 25th, 2019 survey yielded an RMSE of 1.21 m in the x direction, 0.48 m in the y direction, and 0.12 m in the z direction. These high-quality products allow for inter-annual comparison of the slump's progression.

Table 5. Image resolution for DSM and orthomosaics

Dates	Drones	DSM resolution	Orthomosaic resolution
22-08-2019	Phantom 4 Pro V2	2.66 cm	1.33 cm
11-09-2019	Phantom 4 Pro V2	5.40 cm	2.70 cm
25-09-2019	Phantom 4 Pro V2	5.94 cm	2.97 cm
20-05-2020	Phantom 4 Pro V2	5.20 cm	2.60 cm
11-06-2020	Phantom 4 Pro V2		
13-07-2020	Phantom 4 Pro V2	5.20 cm	2.60 cm
26-08-2020	Matrice 210 RTK, Zenmuse x7	2.29 cm	1.14 cm
29-09-2020	Matrice 210 RTK, Zenmuse x7	2.36 cm	1.18 cm

To better understand the morphological characteristics of the site, historical aerial and satellite imagery were analyzed, along with current UAV-derived orthoimages and models.

Aerial and satellite imagery analyses suggest that the thaw slump was instigated in 2014 by the erosion of the Takhini River. Using this imagery in combination with UAV-derived orthoimages has allowed for the progression of the slump to be monitored. According to this analysis, the ongoing thaw of exposed ice has caused the headwall to retreat towards the Alaska Highway at rates of up to 8 m/year since 2014 to its current position 55 m downslope from the highway (Table 6, Figure 33). At present, the thaw slump has a 70-m wide crescent-shaped source zone, with a steep headwall up to 7 m high which

exposes ice-rich permafrost within glaciolacustrine silt and clay sediments. Groundwater springs can be observed seeping from the headwall at several locations between 2-3 metre depth. As thaw debris accumulate at the base of headwall, they are mobilized by mudflows that have travelled upwards of 100 m. On September 2nd 2019, a large mudflow event deposited a low-angle tongue of debris more than halfway across Takhini River (Figure 33).

Table 6. Measured rate of expansion of the retrogressive thaw slump since 2016.

Date	Distance to road (m)	Full size area (m^2)	Area to straight river bank (m^2)
7/27/2016	105.8	1321.9	1257.8
8/18/2018	80.9	2816.3	2705.8
5/16/2019	80.9	N/A	N/A
8/22/2019	71.8	4777.8	4018.5
9/11/2019	69.7	6652.4	4355.5
9/25/2019	68	6942.5	4524.8
10/30/2019	68.8	6816.1	4324.6
5/20/2020	68	6982.9	4590.7
8/26/2020	57.5	7453.2	5466.7
9/29/2020	55.1	7462.02	5499.65

Older aerial imagery shows that two retrogressive thaw slumps of similar size have occurred on the slope adjacent to the current slump. One slump was located 100 m to the west and was active in the 1940s. Another slump was located 200 m to the east and was active from 1979 to 1989. This slump caused tension cracks in the highway embankment. These older slumps have since stabilized, most likely due to depletion of ground ice and/or covering and insulation of their headwalls.

Surface tension cracks up to 1.4 meters deep and 1.8 meters wide have developed adjacent to and upslope from the slump (Figure 33), indicating widespread slope instability that extends beyond the footprint of the slump, likely due to creep or solifluction processes. Tree roots and split trunks extend across the tension cracks in several locations (Figure 33). The crack widths of twelve split trees shown in Figure 34 were remeasured at regular intervals throughout the summer and fall of 2019, with cracks expanding at rates of up to 1-2 cm/month.

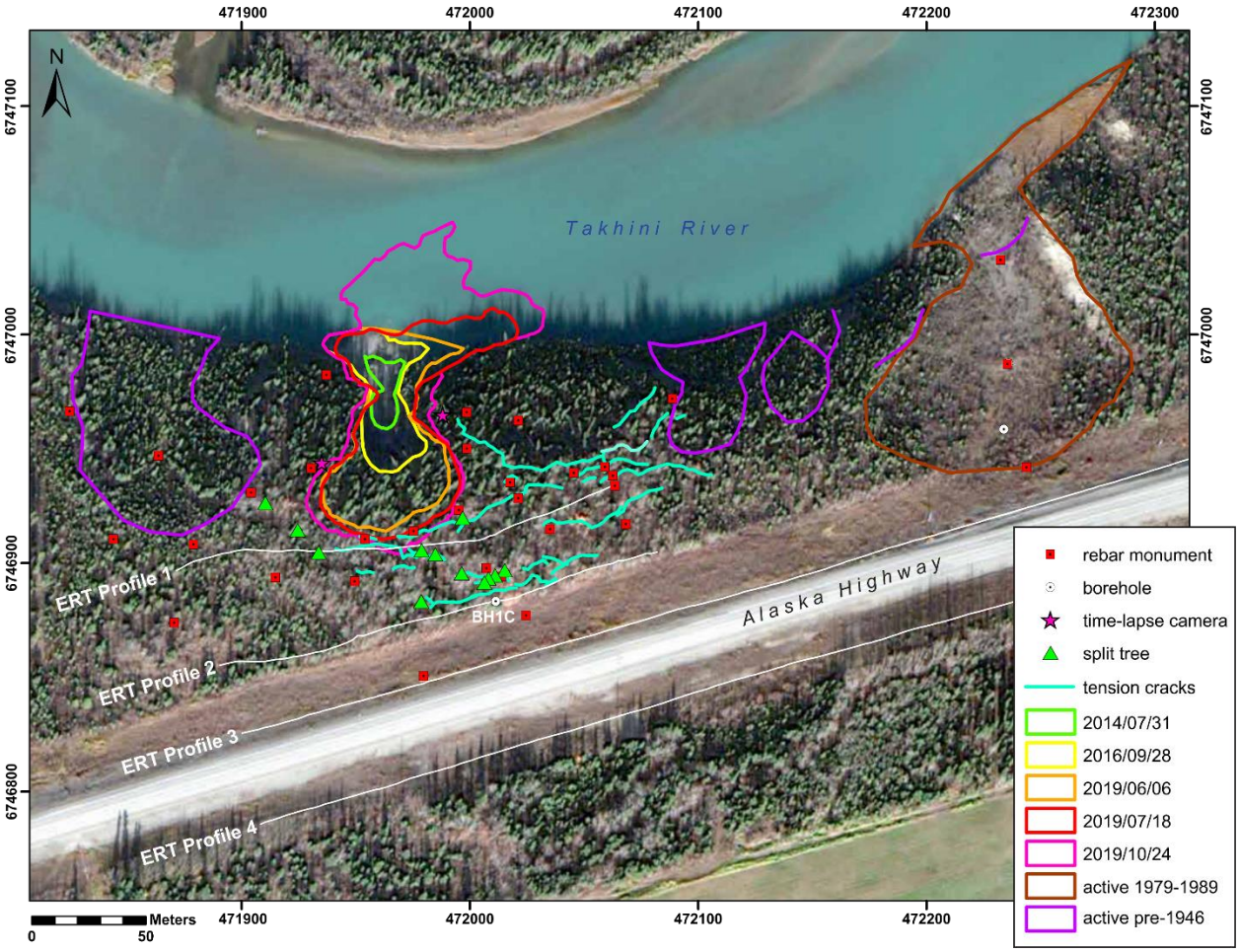

Figure 33. Map of past retrogressive thaw slumps, also showing tension cracks and split trees locations

Figure 34. Split trees due to tension cracking

The ongoing UAV surveys will allow for extremely high-precision and high-accuracy monitoring of ongoing slump progression at regular intervals. As the slump progresses towards the Alaska Highway, this monitoring will be invaluable

4.3.2. Benchmark survey

The benchmark survey allowed for an assessment of error in the DGPS system, which was low in the x-direction, and higher in the y-direction (downslope). Furthermore, the analysis showed that movement was more prevalent in the eastern portion of the slump area (Figure 35). These movements are early indicators that this entire zone may eventually merge with the current retrogressive thaw slump.

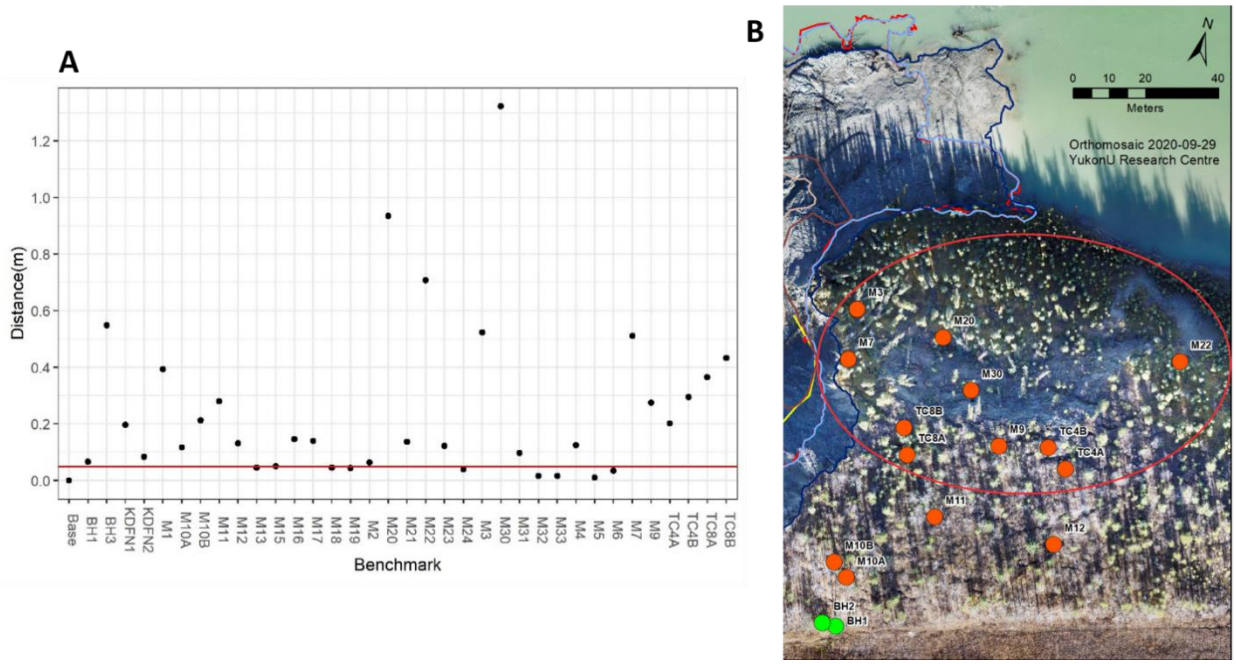

Figure 35. A) Benchmark movement as of September 29th, 2020. Red line corresponds to the point movement vs. $\overline{\boldsymbol{SDy}}$. B) Benchmark monument zone (red circle) associated with the most movement

5. Synthesis of results

5.1. General permafrost characteristics and history

The geotechnical boreholes and ERT data are consistent in defining the top and thickness of permafrost (2-3 m depth). The cores collected on site show the presence of clayey silts, which are frost susceptible, down to at least 25 metres depth. The temperature data recorded suggest that the permafrost is warm, close to 0°C, and therefore vulnerable to thaw. The geophysical and geotechnical data showed thick, ice-rich permafrost at the headwall of the thaw slump and more sporadic clusters of ice-rich permafrost closer to the road. This could be explained by decades of permafrost degradation under the right of way of the Alaska Highway since its construction in 1942. However, the ERT data suggest that permafrost could still be present on the southern side of the highway.

Current warm ground temperatures (just below 0°C) and the distribution of ice rich permafrost in clusters (observed in the ERT surveys) seem to indicate that the permafrost

may have formed in a colder and more humid environment than the one prevailing today. The lack of thick organic cover and the abundance of deciduous trees on site is atypical when considering other similar ice-rich epigenetic permafrost in discontinuous areas. This atypical environment suggests that the permafrost may have originally formed under different environmental conditions, associated to a different climate and different vegetation. Therefore, the site might be underlain by relic permafrost that is precariously in balance with the current climate.

The cryostratigraphical observations from the core samples and the headwall are consistent with syngenetic permafrost. The formation of this type of ground ice, with suspended and thick layered cryostructure in fine grained material, requires ample water supply, a slow thermal gradient, and usually an organic cover. This type of permafrost is generally associated with permafrost plateaus and frost heave mound environments (Calmels et al, 2008). Such conditions may have existed in the Takhini Valley when the permafrost developed. Although the vegetation and the topography have changed, the original cryostratigraphical imprint, shown by the ERT survey in the shape of ice-rich ground clusters, has remained unchanged. The shading provided by the newer deciduous forest may have contributed to the preservation of this relic permafrost.

The headwall of the retrogressive thaw slump provides an exceptional view of the ground profile. It shows lacustrine deposits (clayey silts) reworked by ground movements (Figure 36), with ice lenses being in unconformity with the stratigraphy yet parallel to the topography. This indicates that the permafrost was formed after the ground disturbances that caused sedimentary reworking.

Figure 36. Retrogressive thaw slump headwall

Figure 37 shows the approximate ground ice distribution based on the ERT profiles. The location of the ice suggests that the study site is vulnerable to further degradation even near the road. It is of note that the location of the inactive slump shows no ground ice, which could explain why this slump stabilized, or alternatively, that any ice present at that location has already melted out with the slump.

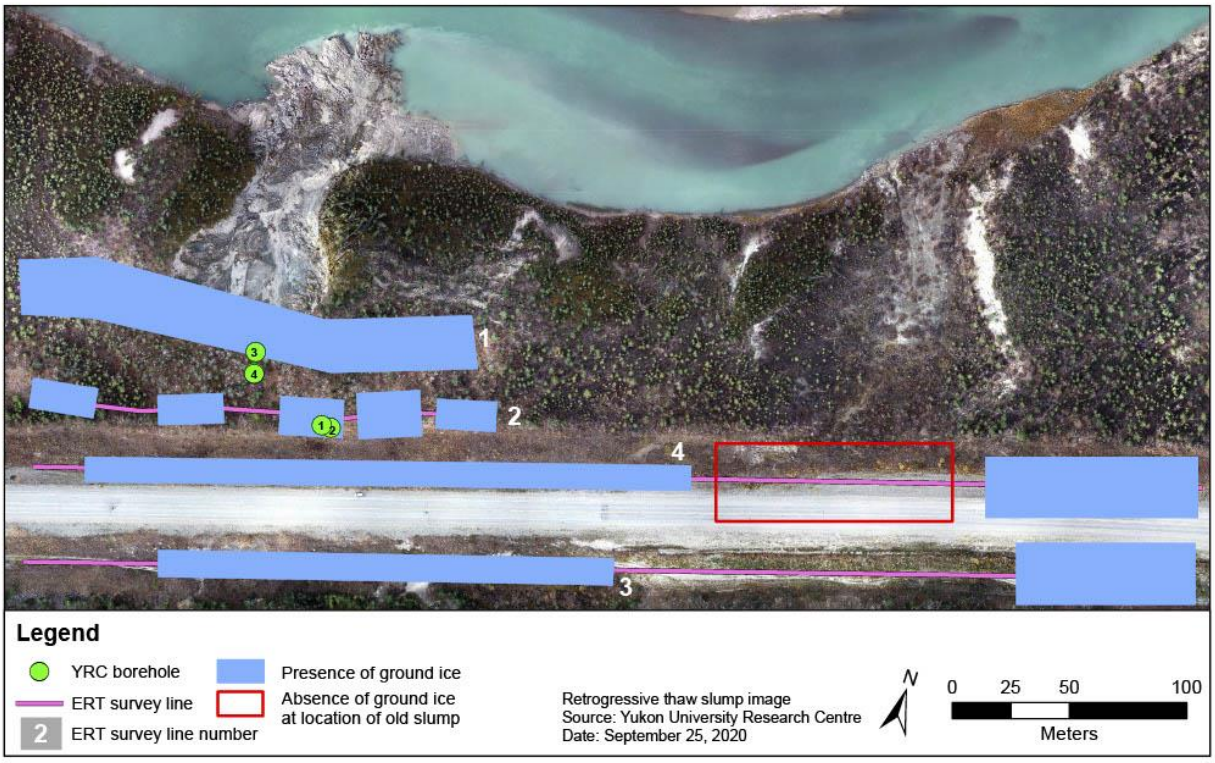

Figure 37. Approximate position of ground ice based on ERT profiles

5.2. Retrogressive thaw slump processes

Geophysical and borehole data emphasize the ice-rich nature of the ground at this site, as well as the presence of ground water flows. While the thaw processes may have been initiated by bank erosion on the Takhini River, they have been exacerbated by the high ground ice content and the thermal effect of ground water springs circulating within the ice-rich clusters as depicted in the 3D ERT models (section 4.2.2). Irrigation of the farmland located on the other side of the highway in the summertime may contribute to the degradation processes.

The ground temperature and inclinometer data show precursory indicators of the RTS failure processes. Temperatures recorded in BH3 show an increase 6 days before the headwall reached the borehole and the pipe collapsed (Figure 38A). Incremental displacement is minimal at the surface (0 m) and 0.5 m depths in BH3 until August 6th. After this, it increases until the failure of the borehole, also 6 days later (Figure 38B and C).

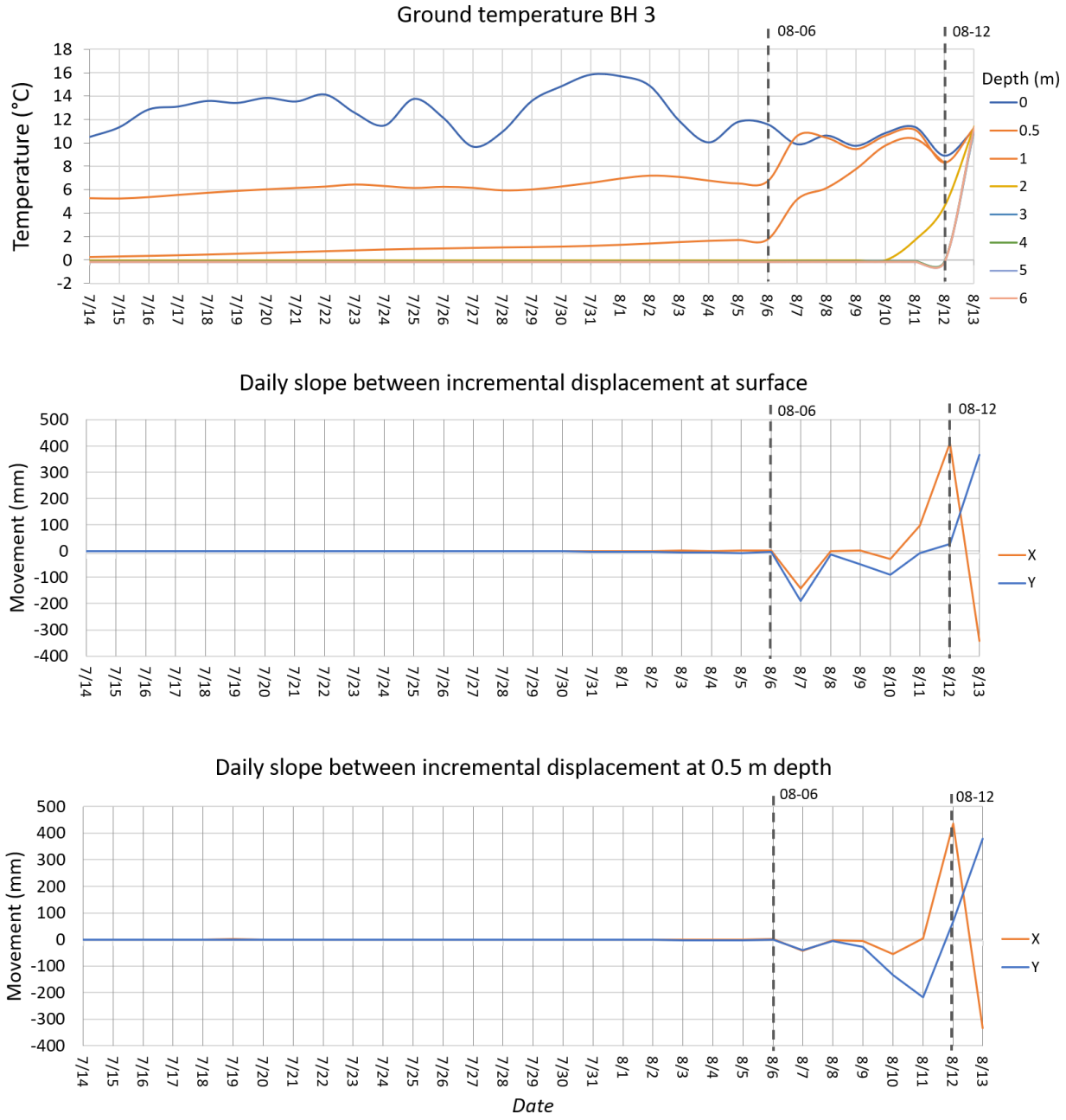

Figure 38. Comparison between ground temperature and displacement recorded by the inclinometer in BH3 at 0 m and 0.5 m, summer 2020

Farther away from the slump at BH2, inclinometer data also show a sudden displacement when the slump gained on BH3. This suggests that the slump eroded in one quick event rather than through slow incremental erosive processes.

All together, these records suggest that ground temperature and inclinometer data could be used as an anticipatory warning of failure for a specific point many days before a catastrophic event. Remote daily monitoring of this data could be used in an alarm system to trigger an alert for an upcoming collapse. Such a system could be used to monitor the thaw slump as it progresses towards the highway and help the highway operator to ensure public safety.

6. References

ASTM Standard C29 – 09, 2000. Standard Test Method Bulk Density ("Unit Weight") and Voids in Aggregate. West Conshohocken, PA, ASTM International.

ASTM Standard D422 – 63, 2000. Standard Test Method for Particle-Size Analysis of Soils. West Conshohocken, PA, ASTM International.Bond, J.D., 2004. Late Wisconsinan McConnell glaciation of the Whitehorse map area (105D), Yukon. In: Yukon Exploration and Geology 2003, Emond, D.S. and Lewis, L.L. (eds.), Yukon Geological Survey, p. 73-88.

Burn, C.R. 1987. Thermokarst ponds and ground temperatures in Takhini Valley. In XIIth INQUA Congress field excursions A20 and A20b Research in Yukon. Edited by S.R. Morison and C.A.S. Smith. National Research Council of Canada, Ottawa, Ont., p. 34.

Burn, C.R. 1998. The response (1958-1997) of permafrost and near-surface ground temperatures to forest fire, Takhini River valley, southern Yukon Territory. Canadian Journal of Earth Sciences. 35: 184-199.

Calmels, F., Allard, M., 2007. Segregated Ice Structures in Various Heaved Permafrost Landforms Through CT Scan. Earth Surface Processes and Landforms, 33, p 209-225, DOI: 10.1002/esp.1538.

Egginton, P., French, H., 1976. Thermokarst and related geomorphic processes eastern Banks Island, N.W.T. University of Ottawa, PhD Thesis. UMI: EC55744.
French, H., 2007. The Periglacial Environment. Third Edition.

Hauck, C., Isaksen, K., Vonder Mühll, D. and Sollid, J.L., 2004. Geophysical surveys designed to delineate the altitudinal limit of mountain permafrost: An example from Jotunheimen, Norway. Permafrost and Periglacial Processes, vol. 15, p. 191-205, doi:10.1002/ppp.493.

Hilbich, C., Hauck, C., Hoelzle, M., Scherler, M., Schudel, L., Voelksch, I., Vonder Muehll, D. and Maüsbacher, R., 2008. Monitoring mountain permafrost evolution using electrical resistivity tomography: A 7-year study of seasonal, annual, and long-term variations at Schilthorn, Swiss Alps. Journal of Geophysical Research-Earth Surface, vol. 113, doi:10.1029/2007JF000799.

Hilbich, C., Marescot, L., Hauck, C., Loke, M.H. and Maüsbacher, R., 2009. Applicability of electrical resistivity tomography monitoring to coarse blocky and ice-rich permafrost landforms. Permafrost and Periglacial Processes, vol. 20, p. 269-284, doi:10.1002/ppp.652.

Hughes, O.L., Pilon, J., Veillette, J.J., Zoltai, S.C., and Pettapiece, W.W., 1973. Three surficial geology and geomorphology maps of Trial river, Bell river, Old Crow map-areas, Mackenzie Valley and northen Yukon Territory. Geological Survey of Canada, Open File 167, 1 sheet. doi:10.4095/129201

Klassen, R.W. 1979. Thermokarst terrain near Whitehorse, Yukon Territory. In Current research, part A. Geological Survey of Canada, Paper 79-1A, pp. 385–388.

Kneisel, C., Hauck, C. and Vonder Mühll, D., 2000. Permafrost below the timberline confirmed and characterized by geoelectrical resistivity measurements, Bever Valley, eastern Swiss Alps. Permafrost and Periglacial Processes, vol. 11, p. 295-304, doi:10.1002/1099-1530(200012)11:4<295::AID-PPP353>3.0.CO;2-L.

Kneisel, C., Hauck, C., Fortier, R. and Moorman, B., 2008. Advances in geophysical methods for permafrost investigations. Permafrost and Periglacial Processes, vol. 19, p. 157-178.

Lewkowicz, A. G., Bonnaventure, P. P., Smith, S. L. and Kuntz, Z., 2012. Spatial and thermal characteristics of mountain permafrost, Northwest Canada, Geografiska Annaler, vol. 94, p. 195–213, doi:10.1111/j.1468-0459.2012.00462.x.

Lewkowicz, A. G., Etzelmüller, B.E. and Smith, S.L., 2011. Characteristics of discontinuous permafrost from ground temperature measurements and electrical resistivity tomography, southern Yukon, Canada. Permafrost and Periglacial Processes, vol. 22, p. 320-342.

Lipovsky, P.S. and Yoshikawa, K., 2009. Initial results from the first year of the Permafrost Outreach Program, Yukon, Canada. In: Yukon Exploration and Geology 2008, L.H. Weston, L.R. Blackburn and L.L. Lewis (eds.), Yukon Geological Survey, p. 161-172.

Lipovsky, P.S., 2015. Summary of Yukon Geological Survey permafrost monitoring network results, 2008-2013. In: YukonExploration and Geology 2014, K.E. MacFarlane, M.G. Nordling and P.J. Sack (eds.), Yukon Geological Survey, p. 113-122.

Loke, M.H. and Barker, R.D., 1996. Rapid leastsquares inversion of apparent resistivity pseudosections using a quasi-Newton method. Geophysical Prospecting, vol. 44. p. 131-152, doi:10.1111/j.1365-2478.1996.tb00142.x
Loke, M.H., Acworth, I. and Dahlin, T., 2003. A comparison of smooth and blocky inversion methods in 2D electrical imaging surveys. Exploration Geophysics, vol. 34, p. 182-187.

Miceli, C., 2012. Seasonal cycling in electrical resistivities at ten thin permafrost sites, southern Yukon and northern British Columbia. Unpublished MSc thesis, Department of Geography, University of Ottawa, ON, 201 p.

Murton, J.B. and French, H.M., 1994. Cryostructures in permafrost, Tuktoyaktuk coastlands, western arctic Canada. Canadian Journal of Earth Sciences, vol. 31, no. 4, p. 737-747.

Smith, M.W. and Riseborough, D.W., 2002. Climate and the limits of permafrost: a zonal analysis. Permafrost and Periglacial Processes, vol. 13, p. 1-15.

Stephani, E., Fortier, D. and Shur, Y., 2010. Applications of cryofacies approach to frozen ground engineering – Case study of a road test site along the Alaska Highway (Beaver Creek, Yukon, Canada). GEO2010: 63rd Canadian Geotechnical Conference and 6th Canadian Permafrost Conference, Calgary, Canada.

Yukon Geological Survey, 2020. Yukon Digital Bedrock Geology. http://www.geology.gov.yk.ca/update_yukon_bedrock_geology_map.html, accessed: 28 January 2021.

7. Appendix A

No 1: Borehole log WH_1456_BH1, with volumetric excess ice content and grain size distribution

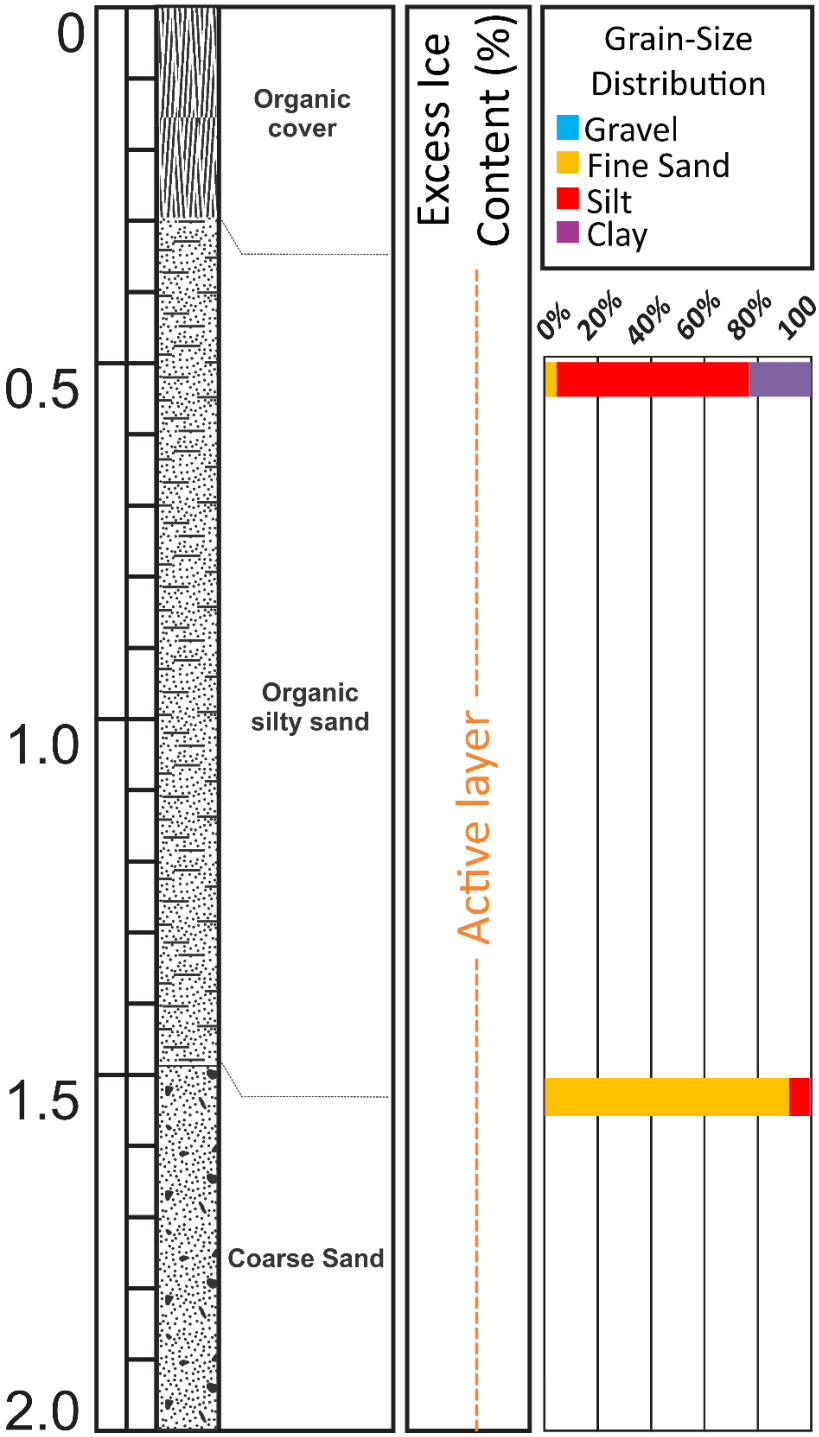

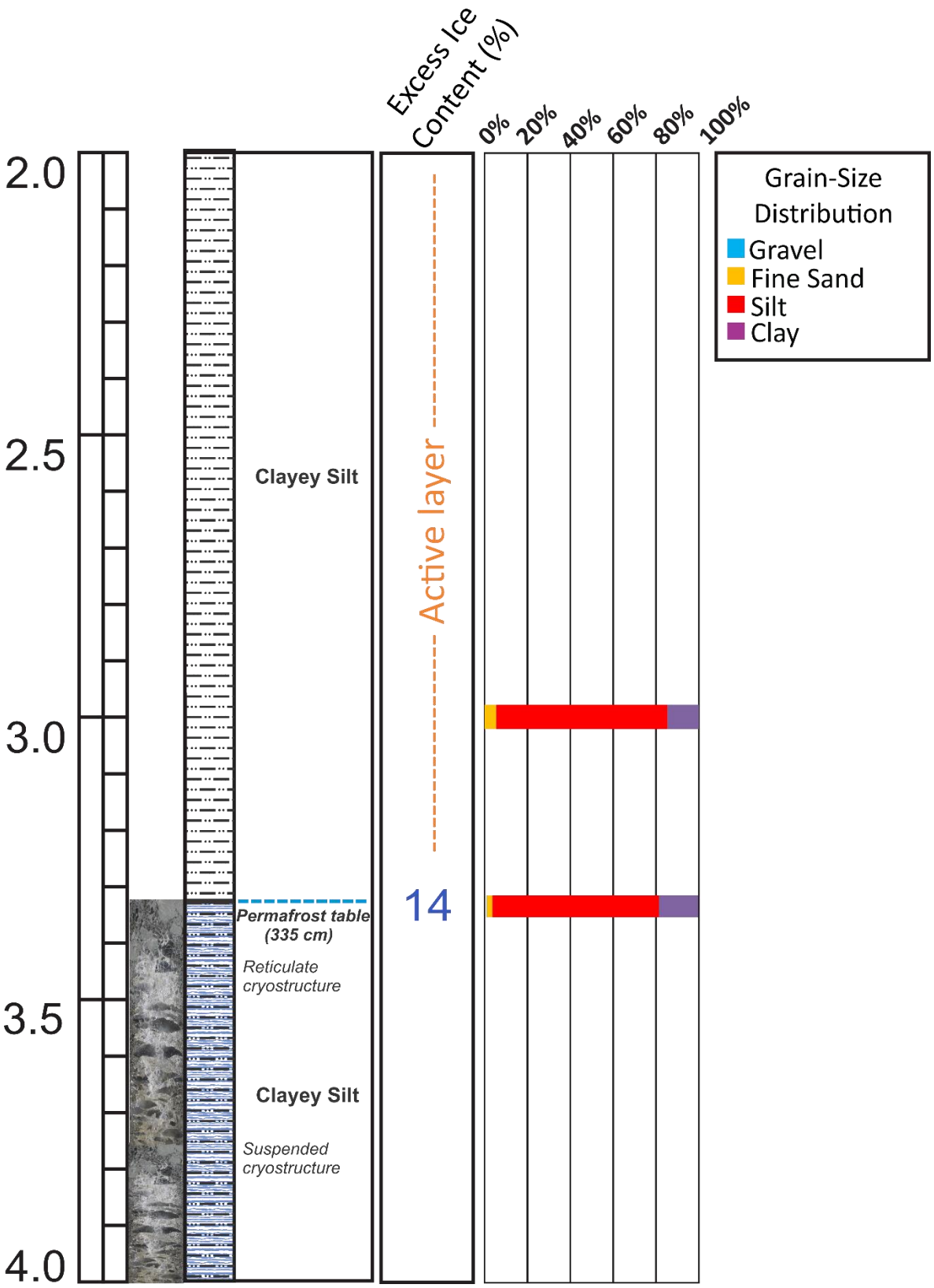
Excess Ice Content (%)
0%
20%
40%
60%
80%
100%
2.0
2.5
3.0
3.5
4.0
Clayey Silt
Active layer
14
Permafrost table (335 cm)
Reticulate cryostructure
Clayey Silt
Suspended cryostructure
Grain-Size Distribution
Gravel
Fine Sand
Silt
Clay

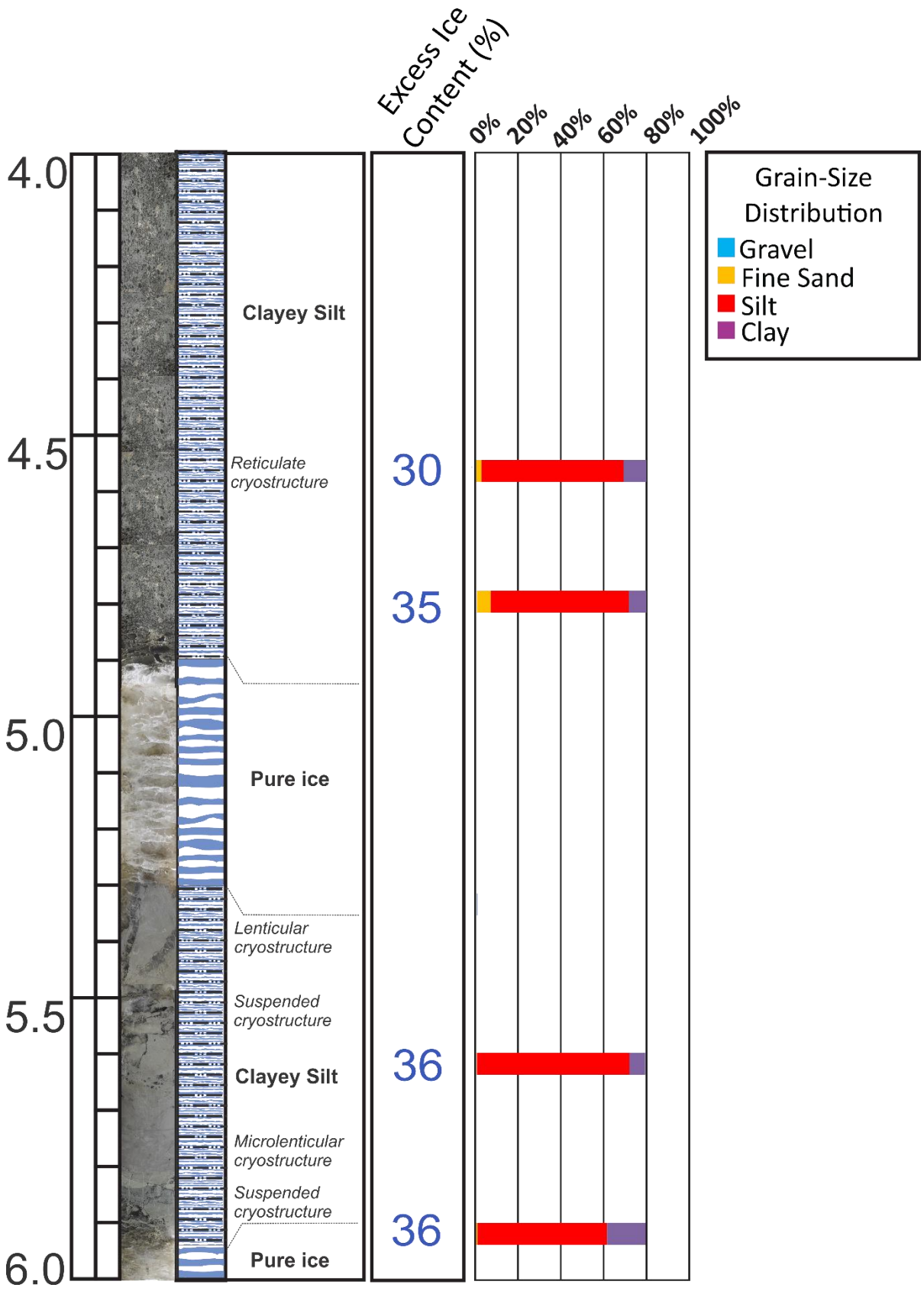
Excess Ice Content (%)
0%
20%
40%
60%
80%
100%
4.0
4.5
5.0
5.5
6.0
Clayey Silt
Reticulate cryostructure
Pure ice
Lenticular cryostructure
Suspended cryostructure
Clayey Silt
Microlenticular cryostructure
Suspended cryostructure
Pure ice
30
35
36
36
Grain-Size Distribution
Gravel
Fine Sand
Silt
Clay

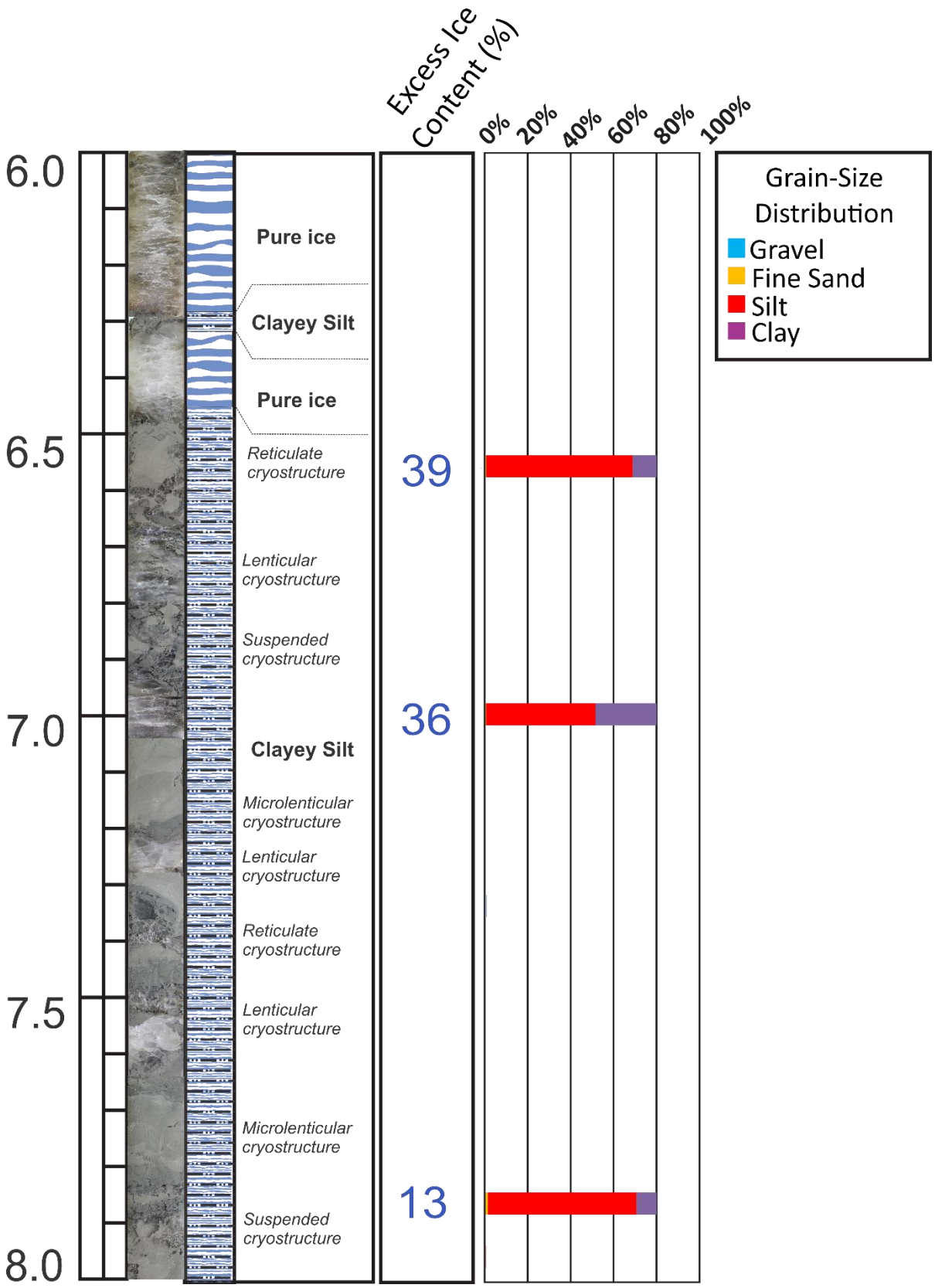
Excess Ice Content (%)
0%
20%
40%
60%
80%
100%
6.0
6.5
7.0
7.5
8.0
Pure ice
Clayey Silt
Pure ice
Reticulate cryostructure
Lenticular cryostructure
Suspended cryostructure
Clayey Silt
Microlenticular cryostructure
Lenticular cryostructure
Reticulate cryostructure
Lenticular cryostructure
Microlenticular cryostructure
Suspended cryostructure
39
36
13
Grain-Size Distribution
Gravel
Fine Sand
Silt
Clay

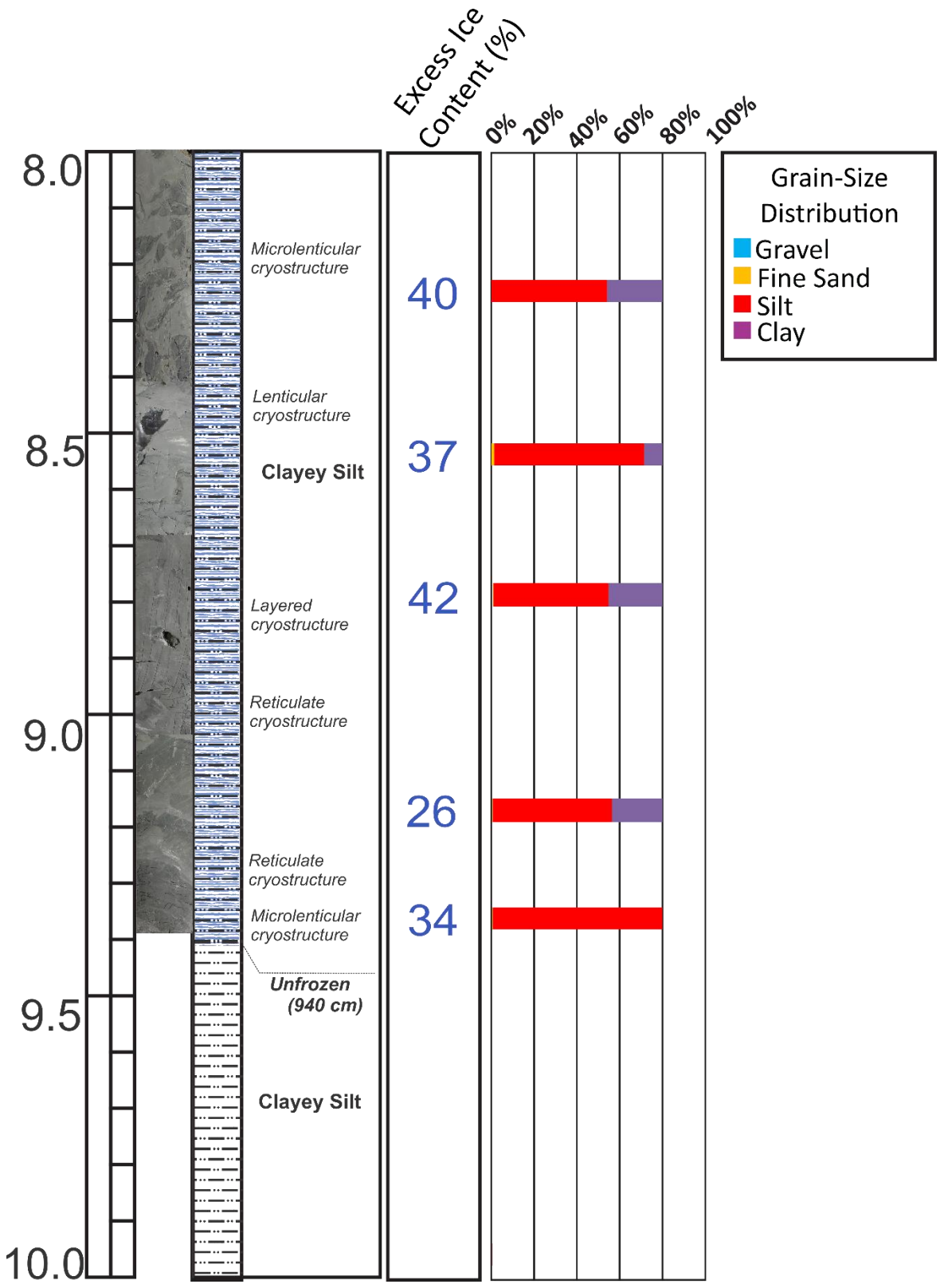

End of Borehole: 10 meters

No2: Borehole log WH_1456_BH3

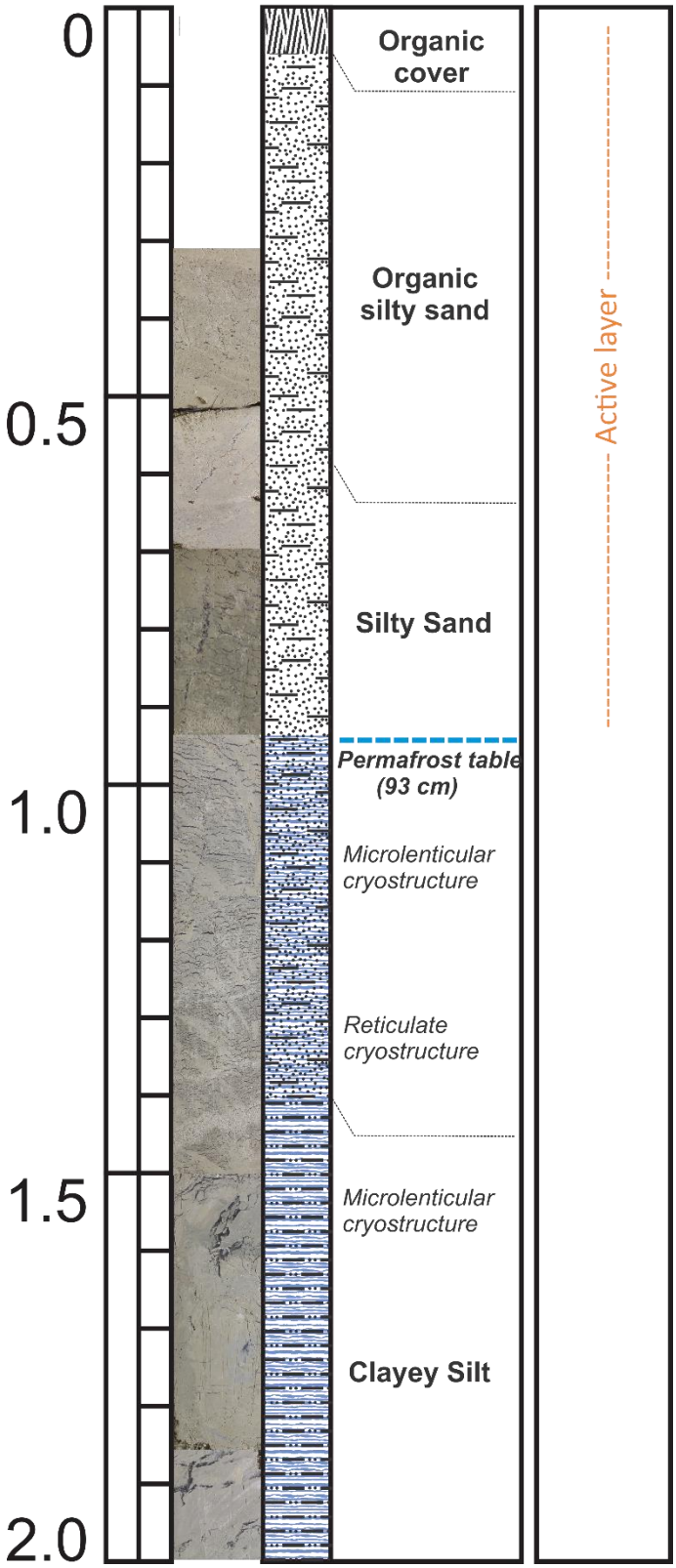

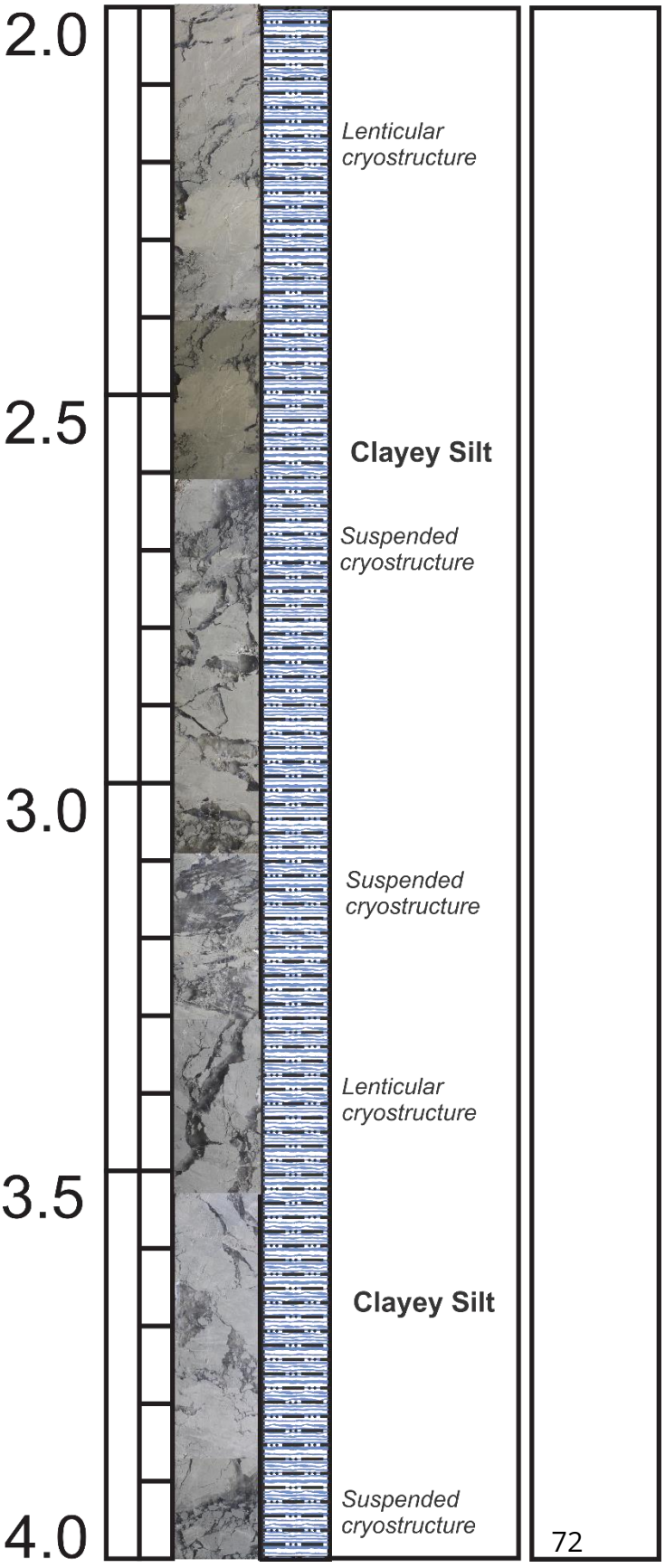
2.0
2.5
3.0
3.5
4.0
Lenticular cryostructure
Clayey Silt
Suspended cryostructure
Suspended cryostructure
Lenticular cryostructure
Clayey Silt
Suspended cryostructure

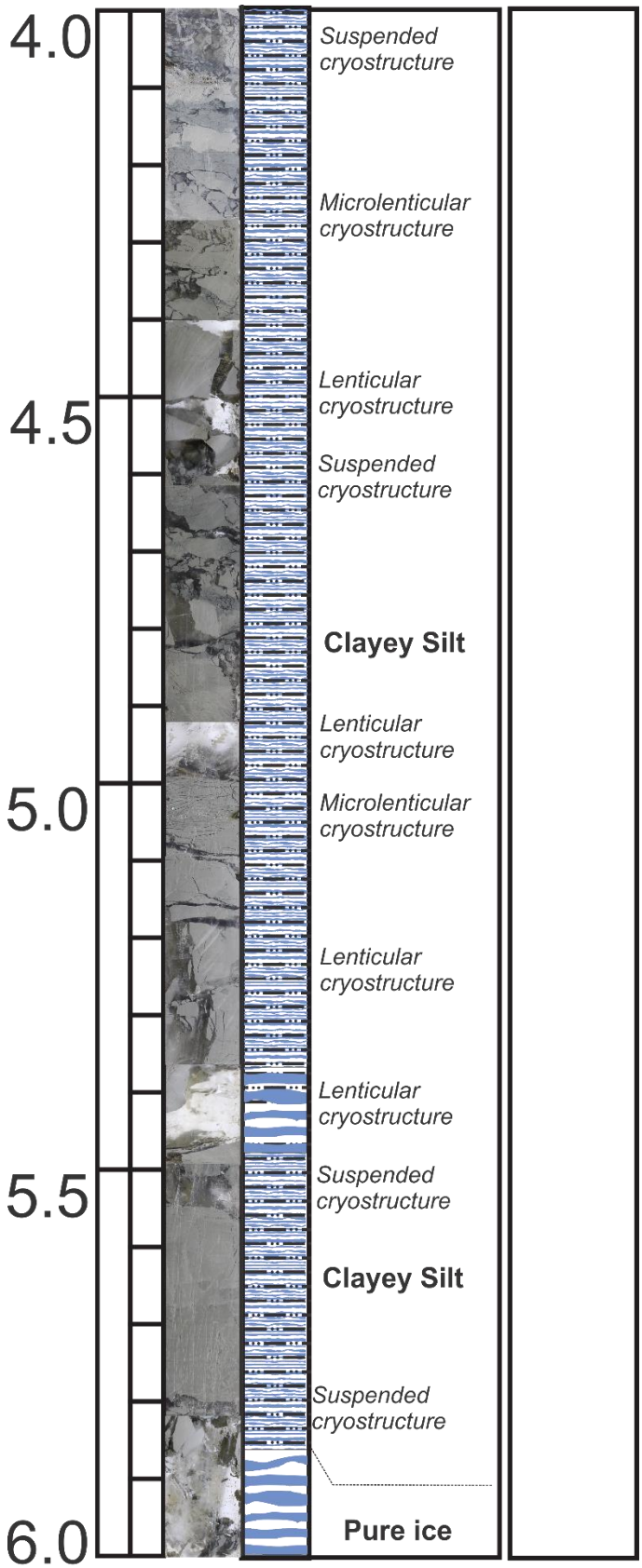

End of Borehole: 6 meters